Cement and Concrete Composites 148 (2024) 105465

Contents lists available at ScienceDirect

Cement and Concrete Composites

journal homepage: www.elsevier.com/locate/cemconcomp

Multiscale and multiphysics discrete model of self-healing of matrix and interfacial cracks in fibre reinforced cementitious composites: Formulation, implementation and preliminary results

Antonio Cibelli *, Liberato Ferrara, Giovanni Di Luzio

Department of Civil and Environmental Engineering, Politecnico di Milano, Piazza Leonardo da Vinci 32, Milan, 20133, MI, Italy

ARTICLE INFO

Keywords:
Self-healing
FRC
UHPC
Concrete
Numerical modelling
Discrete model
Multiscale model
LDPM
HTC
Durability

ABSTRACT

This paper focuses on the numerical modelling of autogenous and stimulated healing of cracks in fibre-reinforced cementitious composites, with the aim of showing the potential that a multiphysics and multi-scale discrete model has in capturing the complex hygro-thermo-chemo-mechanical processes governing concrete ageing and its capability of autonomously repairing cracks.

This study expands a prior research on numerical modelling of self-healing of normal-strength concrete, to simulate the autogenous and stimulated healing of cracks in fibre-reinforced cement-based composites. The proposed extended model explicitly differentiates between (i) major cracks in the cementitious matrix and (ii) debonding cracks at matrix–fibre interface.

The increased fibre-matrix bond due to the healing products along the interface cracks is explicitly implemented to capture the possibility of having a healing-induced mechanical recovery even when major cracks are totally or partially unhealed, complying with experimental evidence available in the literature. The model can also simulate the material ageing. After the model formulation and implementation in the Multiphysics-Lattice Discrete Particle Model (M-LDPM) framework, an example of calibration and validation for one of the Ultra High Performance Concrete (UHPC) mixes developed within the Horizon 2020 project ReSHEALience is presented.

1. Introduction

Steel-reinforced concrete is the most widely used construction material due to its affordability and good mechanical performance for structural purposes. However, the cracking and degradation caused by increased permeability in the cracked state affects its durability [1]. Short fibres – made of steel, polymers, carbon, glass or natural vegetable materials – can replace conventional reinforcement in concrete to improve structural behaviour [2]. They result in narrower and closely spaced cracks, which increase fracture toughness and ductility, and reduce the damage caused by penetrating aggressive agents [3,4].

Having multiple smaller cracks is not the only strategy to tackle the need for more durable concrete structures. Ultra high-performance concrete (UHPC) usually features an engineered mix composition, in which the dosages and nature of each compound are driven by performance requirements and the will to have a wiser usage of raw materials. Using by-products as partial replacements for aggregates and cement is gaining popularity as a sustainable approach.

Narrower cracks have been proven to self-heal better and faster [5]. Autonomous maintenance - throughout the life of a structure and as soon as the damage occurs - is expected to best express in *advanced* fibre reinforced cementitious composites [6].

In recent years, self-healing materials have gained more and more attention. They can be subdivided in three categories: (i) *autogenous*, which contains no healing agents; (ii) *stimulated autogenous*, which contains tailored chemical additives to promote healing (e.g., crystalline admixtures [7]); and, (iii) *engineered*, which includes cement-based materials with added compounds to activate healing reactions [8]. Examples include concrete with embedded capsules [9–11] or vascular systems [12–15] filled with healing agents. When cracks appear, the capsules or vascular network rupture, releasing the healing agent into the crack.

The modelling approach presented in this article deals with autogenous and stimulated healing. Aldea et al. [16], through non-destructive tests, and Ferrara et al. [17], employing a customised *fracture testing*-based approach, investigated the autogenous and stimulated healing capacity of normal strength concretes for crack widths ranging between 50 to 250 μm. They explained the difference between crack *sealing*

* Corresponding author.
E-mail address: antonio.cibelli@unina.it (A. Cibelli).

https://doi.org/10.1016/j.cemconcomp.2024.105465
Received 31 August 2023; Received in revised form 29 December 2023; Accepted 31 January 2024
Available online 6 February 2024

(recovery in water tightness) and crack *healing* (recovery in stiffness and strength). However, ordinary concrete typically does not experience significant healing through sealing, even in the presence of wide cracks [16,18,19]. The recovery in strength is not negligible when the cracked samples are cured in saturated conditions, for long periods [17]. Some years later, Lo Monte and Ferrara [20] confirmed those results showing that the adoption of strain-hardening fibre reinforced cementitious composites promotes self-healing phenomena, thanks to smeared cracking with low crack openings, ranging from 10 to 50 μm. In addition, relevant to UHPC, Cuenca et al. [6,21,22] investigated the synergy between crystalline admixtures and nano-constituents, providing insightful evidence on the enhancement and speed-up that the latter induce on the healing process. Fan and Li [23] adopted the micro-tomography to analyse how the crack width affects the formation of healing products. The authors showed that small cracks heal easier near the tips, while larger cracks allow water to seep in for longer periods, resulting in more extensive healing. They also proved that mechanical recovery depends on 3D spatial development, not just surface-level crack closure.

In the Horizon 2020 project ReSHEALience, led by Politecnico di Milano, delivered – among other results – the definition of a new concept of ultra-high performance cementitious material, the Ultra High Durability Concrete (UHDC) [21]. It presents an optimised mix, including slag as supplementary cementitious material, steel fibres, and additives to enhance the self-healing capacity. Different UHDC prototypes were tested in the laboratory to characterise their mechanical and physical properties. In addition, six pilot applications were realised and monitored as proofs-of-concept [24–27]. They were exposed to different extremely aggressive environments (e.g., off-shore structures, geothermal power plants) to compare their response to the environmental agents with that of reinforced concrete in use today. The developed model, presented in this work, points towards the ambitious yet highly needed goal of having a comprehensive model for the durability of concrete structures. This research demonstrates the potential of a multi-scale and multi-physics model in capturing complex processes governing concrete ageing and autonomously repairing cracks. Furthermore, the model is suited to simulate the behaviour of advanced cementitious composites. Its flexible numerical architecture allows it to include the effect of other constituents not considered so far. That might be an interesting opportunity for the design of *innovative* purpose-oriented cementitious composites, whose physical and mechanical response could be preliminarily simulated in order to improve the engineering and optimisation stages [28].

The modelling of concrete healing is a topic which has been recently gathering an increasing interest within the scientific community [29]. There are some modelling approaches in the literature, such as (i) a model coupling mechanical, hydraulic, and chemical aspects to evaluate the mechanical properties of the healing products, based on observations at the microscale [30]; (ii) a finite element model, based on the coupling of the microstructural hydration model CEMHYD3D and the finite element code Cast3M [31]; (iii) an uncoupled chemo-physical model formulated on the hypothesis that the healing mechanism is triggered by $CaCO_3$ (calcium carbonate) precipitation within the cracks [32]; (iv) a constitutive model simulating the healing process at the microscale through the solidification theory [33]. However, each model presents some simplifying assumptions. An alternative to the afore-mentioned approaches is represented by the so-called Continuum Damage-Healing Mechanics (CDHM) [34–36], which has been recently extended to cementitious materials showing interesting perspectives [37,38]. In the CDHM, a thermodynamically-wise consistent framework is preserved, and additional internal variables are introduced to account for the healing effects. Barbero et al. [34], Schimmel and Remmers [35] presented a dedicated formulation for fibre reinforced polymer–matrix composites, however without a proper validation against experimental evidence. Di Luzio et al. [5] proposed to model the mechanical regain due to the healing of cracks through a coupled approach, relying on pairing the Solidification-Microprestress-Microplane (SMM) model [39] with the Hygro-Thermo-Chemical (HTC) model [40]. The resulting continuum-based approach showed the capacity of capturing the healing-induced effects on the mechanical response in the cracked state. The model was calibrated and validated for damaged plain concrete exposed to saturated and open air conditions. In addition to the above-mentioned approaches, Yang et al. [41] assessed the feasibility of applying the Phase-Field Methods to model the mechanical recovery of healed quasi-brittle materials. Recently, promising results have been achieved by Jefferson and Freeman [42], which proposed an approach based on a discrete multi-ligament model, enabling the simulation of simultaneous cracking–healing responses in systems that exhibit significant COD and COD-rate effects. Using cohesive crack models, some investigators have also analysed healing in discrete cracks of quasi-brittle materials, such as [43,44].

Most of the aforementioned modelling approaches assume healing effects on mechanical properties as a smeared contribution in the cracked state. Consequently, they are unable to replicate local phenomena, e.g., where the water permeability increases dramatically and restores after healing, the recovery of fibre carrying-load capacity due to the healing-induced improved friction between the steel element and the surrounding matrix, etc. In 2022, a multi-scale discrete model for both autogenous and stimulated autogenous healing in ordinary cementitious materials was presented [45]. The discrete modelling, based on the Multiphysics-Lattice Discrete Particle Model numerical framework [46–51], enables a realistic simulation of crack patterns and chemical reactions ongoing along the crack walls.

To the best of the authors' knowledge, a model to simulate the healing effect on the mechanical response of fibre-reinforced concretes is still missing in the literature. For this reason, and concerning the model presented by Cibelli et al. [45], a step forward is made in this work. The above-mentioned model has been extended to simulate the autogenous and stimulated (autogenous) healing of cracks in fibre-reinforced cement-based composites at two different scales, explicitly differentiating between (i) major cracks in the cementitious matrix and (ii) debonding cracks at matrix–fibre interface. Furthermore, the parallel track is also kept in the mechanical modelling. The increased fibre-matrix bond due to the healing products along the interface cracks is explicitly implemented to capture the possibility of having a healing-induced mechanical recovery even when major cracks are totally or partially unhealed, as highlighted by Qiu et al. [52]. The model can also simulate the material ageing [28]. Therefore, after proper calibration, it can capture not only the mechanical recovery due to autogenous and stimulated healing in cracked conditions but also the time evolution of stiffness and strength from an early age onwards. The proposed model in its development stages was presented at some recent conferences [53–56].

In the next sections, the model is presented after a brief overview of the M-LDPM numerical framework, followed by an example of calibration and validation for one of the UHDC prototype mixes developed within the Horizon 2020 project ReSHEALience.

2. Multiphysics-Lattice Discrete Particle Model

In Multiphysics-Lattice Discrete Particle Model (M-LDPM) the numerical architecture of Lattice Discrete Particle Model (LDPM), first published by Cusatis et al. [57], is used as basis for the discrete formulation of Hygro-Thermo-Chemical (HTC) model, presented by Di Luzio and Cusatis [40] to simulate the transport phenomena of moisture and heat, together with chemical activity, in cementitious materials. The discrete implementation of the HTC model is performed through the definition of a lattice system, namely a network of flow lattice elements (FLEs), which are anchored to the nodes of the existing LDPM mesh (Fig. 1). This approach enables an easier coupling between mechanical and chemo-diffusion problems.

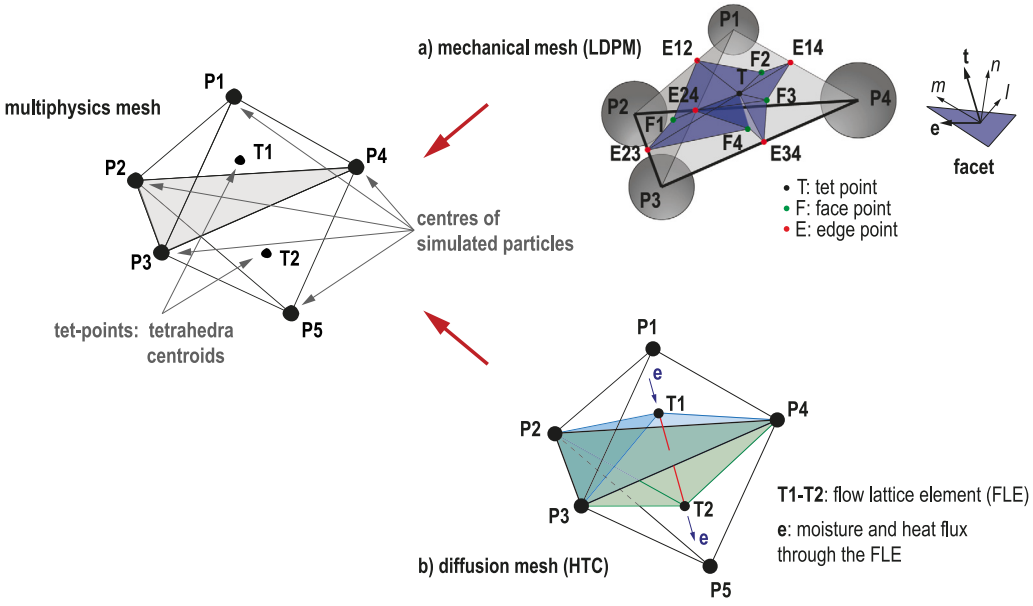

Fig. 1. M-LDPM – Mechanical and diffusion meshes.

Flow Lattice Element (FLE) simulates a channel collecting moisture and heat fluxes between two adjacent tetrahedra [51]. As shown in Fig. 1, it connects two points inside two adjacent tetrahedra (tet-points), which are also vertices of the corresponding polyhedral cells. Then, the transport phenomena within the whole domain are simulated employing a network of FLEs connecting all the tetrahedra. The environmental conditions are applied through a dedicated external layer of edge elements.

LDPM-HTC coupling relies on the implementation of a 10-step algorithm, presented in detail by Cibelli et al. [28]. Numerical mechanical analyses are generally performed in the time scale of micro- or miniseconds. On the other hand, diffusion analyses (e.g., curing, ageing) typically refer to significantly larger time scales (i.e., days, months, or years). Relevant to hygro-thermo-chemo-mechanical models, as M-LDPM, it is impossible to adopt the same time step for both mechanical and diffusion problems. In M-LDPM, this issue is addressed by means of a time map, which scales down the time scale of the HTC analysis to ensure a reasonably small time step for the LDPM simulations.

The idea on which the above-mentioned algorithm is built consists of having – at each time step – both LDPM and HTC parameters updated with a two-way information exchange between the two sides of the multiphysics problem. On one side, LDPM parameters, namely the mechanical properties, are updated depending on the environmental boundary conditions and the material age. Symmetrically, the moisture diffusion in HTC is updated to account for the effect of crack opening computed through LDPM analyses. In this numerical architecture, the self-healing model is framed. As a matter of fact, autogenous healing affects, at the same time, the moisture permeability (i.e., crack sealing) and the mechanical performance in the cracked state (i.e., crack healing).

The two-way coupling relies on sharing information between HTC and LDPM solving loops. In particular, *ageing degree* and *crack opening* are used as *bridging* parameters, as it is presented in the following, after an overview of LDPM and HTC models.

2.1. Lattice Discrete Particle Model

Lattice Discrete Particle Model has been shown to be able to accurately simulate the mechanical behaviour of cement-based materials, such as concrete and mortar [50,57–59], and fibre-reinforced concrete [60–62]. The material is modelled at the mesoscopic scale, at which it can be seen as a two-phase composite: coarse aggregates and embedding matrix.

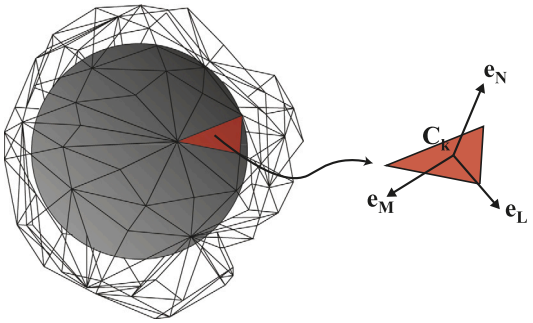

Fig. 2. LDPM — Polyhedral cell and triangular facet.

LDPM mesh derives from the *Delaunay tetrahedralisation* of a system of points, namely particles' centres, placed into the domain through a trial-and-error random procedure, and whose size distribution is obtained from a *Fuller*- or *Bolomey*-type particle size distribution curve. Afterward, a *tesselation* is performed to identify triangular *facets*, representing the cross-section of the lattice elements (i.e., tetrahedra edges). The result is a system of polyhedral cells, mechanically interacting through the above-mentioned facets (Fig. 2).

The deformation of the lattice particle system is described by means of the rigid body kinematics. In this perspective, the displacement step $[\![\mathbf{u}_C]\!]$ at the centroid of the kth projected facet, C_k, is used to define the strain measures: $\varepsilon_N = \left(\boldsymbol{n}^T[\![\mathbf{u}_C]\!]\right)/l$, $\varepsilon_L = \left(\boldsymbol{l}^T[\![\mathbf{u}_C]\!]\right)/l$, and $\varepsilon_M = \left(\boldsymbol{m}^T[\![\mathbf{u}_C]\!]\right)/l$, where $\boldsymbol{n}$, $\boldsymbol{l}$, and $\boldsymbol{m}$ are the unit vectors identifying a local reference system on each facet in normal and shear directions, respectively. The subscripts N, M, and L indicate the strain components along the aforementioned directions. At the centroid of each projected facet, mesoscale vectorial constitutive laws are defined. In the formulation, the facets projected into planes orthogonal to the edges are used to avoid non-symmetric behaviour under pure shear. This issue is clarified in more detail by Cusatis et al. [57].

In the elastic regime, normal and shear stresses are proportional to the corresponding strains. Then, stresses are computed as $\sigma_N = E_N\varepsilon_N^*$, $\sigma_L = E_T\varepsilon_L^*$, and $\sigma_M = E_T\varepsilon_M^*$, where the subscripts N, M, and L maintain the same presented above, while ε_N^*, ε_L^*, ε_M^* are the

strain components net of mesoscale eigenstrains that might arise due to thermal expansion, creep, and shrinkage Wan et al. [46],Alnaggar et al. [47],Abdellatef et al. [63]. The normal and tangential moduli, E_N and E_T, are equals to E_0 and αE_0, respectively, where E_0 is the effective normal modulus, whereas α represents the shear-normal coupling parameter.

At a facet under tension, the mesoscale crack opening, starting to occur when the strain reaches the tensile elastic limit, is expressed by the vector $\boldsymbol{w_c} = w_N \boldsymbol{n} + w_L \boldsymbol{l} + w_M \boldsymbol{m}$, where $w_N = l(\varepsilon_N - \sigma_N/E_N)$ is the opening/closure of the crack along the direction orthogonal to the facet, while $w_L = l(\varepsilon_L - \sigma_L/E_T)$ and $w_M = l(\varepsilon_M - \sigma_M/E_T)$ are two sliding components, catching shear displacements at crack surfaces.

In the mesoscale, three non-linear phenomena govern the material response beyond the elastic limit: (i) fracture and cohesion, (ii) compaction and pore collapse, and (iii) friction. The inelastic behaviour modelling relies on the definition of effective strain $\varepsilon = \sqrt{\varepsilon_N^2 + \alpha\left(\varepsilon_L^2 + \varepsilon_M^2\right)}$ and stress $\sigma = \sqrt{\sigma_N^2 + \left(\sigma_L^2 + \sigma_M^2\right)/\alpha}$, which are employed to formulate damage-type constitutive laws reported in Appendix A.

The extension of LDPM to include discrete dispersed fibre reinforcement is obtained by inserting straight fibres, with random positions and orientations, into the LDPM geometrical configuration. The geometry of each individual fibre is characterised by the diameter d_f (cross-section $A_f = \pi d_f^2/4$) and length L_f. For a given total fibre volume fraction V_f, the number of fibres N_f contained in a specimen volume (V_{sp}) is determined by $N_f = \lceil (V_{sp}V_f)/(A_f L_f) \rceil$ where $\lceil \cdot \rceil$ indicates the ceiling function, which maps to the least integer greater than or equal to $(V_{sp}V_f)/(A_f L_f)$.

The fibre system is overlapped with the polyhedral cell system, and each facet is paired with its intersecting fibres. At the facet level, the matrix–fibre interaction is described by the bridging forces carried by the fibres crossing the facet, which are activated when the crack opening initiates. In this configuration, equilibrium considerations allow to reasonably assume a parallel coupling between the fibres and the surrounding concrete matrix. Then, the total stresses on each LDPM facet can be computed as $\sigma = \sigma_c + \frac{1}{A_c}\sum_{f \in A_c} \boldsymbol{P}_f$, where A_c is the facet area, and $\boldsymbol{P}_f$ represents the crack-bridging force for each fibre crossing the given facet.

The mechanical interaction between the fibres and the surrounding matrix occurs at a scale smaller than the typical modelling scale of LDPM, which is in the order of magnitude of millimetres and is governed by the size of the coarse aggregates in the mixture. For this reason, the micromechanic governing such interaction is not explicitly simulated in the mesoscopic LDPM numerical framework. The micromechanical crack-bridging mechanisms, featuring the bond between the single fibre and the embedding matrix, are implemented into the model within the formulation for computing the bridging force $\boldsymbol{P}_f$, as discussed in detail by Schauffert and Cusatis [60], to which any interested readers can refer, and briefly presented in Appendix B.

2.2. Hygro-Thermo-Chemical model

This model analyses the moisture and heat response of cement-based materials affected by environmental conditions and chemical reactions during curing. The model has been recently improved to account for the effect of slag on material curing [28]. The updated field equations read

$$\nabla \cdot \left(D_h \nabla h\right) = \frac{\partial w_e}{\partial h}\frac{\partial h}{\partial t} + \frac{\partial w_e}{\partial \alpha_c}\dot{\alpha}_c + \frac{\partial w_e}{\partial \alpha_{sl}}\dot{\alpha}_{sl} + \dot{w}_n \tag{1a}$$

$$\nabla \cdot (\lambda \nabla T) = \varrho\, c_t \frac{\partial T}{\partial t} + \dot{\alpha}_c\, c\, \tilde{Q}_c^{\infty} + \dot{\alpha}_{sl}\, sl\, \tilde{Q}_{sl}^{\infty} \tag{1b}$$

Relative humidity h and temperature T are two state variables, whereas α_c and α_{sl} are internal variables, expressing the ratios between the amount of hydrated cement and slag, and the respective total initial contents. Being the cement hydration and slag reaction two diffusion-driven processes, the reaction degrees in rate form can be formulated through Arrhenius-type laws, as reported in Appendix C.

The expression in Eq. (1)a represents the water mass conservation. In the left-hand term, the divergence of the moisture flux, $-\partial w/\partial t = \nabla \cdot \boldsymbol{J}$, is combined with the first Fick's law $\boldsymbol{J} = -D_h(h,T)\nabla h$, with $D_h(h,T)$ moisture permeability coefficient. On the right-hand side, instead, accounts for the contributions of (i) sorption/desorption isotherm ($\partial w_e/\partial h \cdot \partial h/\partial t$), (ii) cement hydration ($\partial w_e/\partial \alpha_c \cdot \dot{\alpha}_c$), (iii) slag reactions ($\partial w_e/\partial \alpha_{sl} \cdot \dot{\alpha}_{sl}$), and (iv) variation of chemically bound water in time ($\dot{w}_n$). The evaporable water content, $w_e = w_e^{gel} + w_e^{cap}$, has two components: (i) the evaporable water in the C-S-H gel w_e^{gel}, and (ii) the capillary water w_e^{cap}. Their formulations are reported in Appendix C, together with the formula of non-evaporable water content w_n.

Concerning the heat transport, Eq. (1)b is the enthalpy balance. The conduction in concrete is described, for temperature lower than 100 °C, by means of Fourier's law: $\boldsymbol{q} = -\lambda \nabla T$, in which $\boldsymbol{q}$ is the heat flux ans λ the heat conductivity. Likewise for moisture, also the enthalpy balance is affected by the chemical reactions occurring from early age onwards.

Finally, the total reaction degree α represents an important parameter in the multiphysics modelling. It combines into a single variable the hydration of cement and slag reaction:

$$\alpha = \frac{\alpha_c \cdot c \cdot \tilde{Q}_c^{\infty} + \alpha_{sl} \cdot sl \cdot \tilde{Q}_{sl}^{\infty}}{c \cdot \tilde{Q}_c^{\infty} + sl \cdot \tilde{Q}_{sl}^{\infty}} \tag{2}$$

where c and sl are the cement slag contents, respectively, $\tilde{Q}_c^{\infty}$ is the cement hydration enthalpy, and $\tilde{Q}_{sl}^{\infty}$ is the latent heat of the slag reaction per unit mass of reacted slag. In the present work it is assumed $\tilde{Q}_{sl}^{\infty} = 800$ kJ/kg [64].

The interested reader may refer to [28,40,65,66] for the detailed description of the HTC formulation, numerical implementation, parameters calibration, and validation.

2.3. Bridging parameters

2.3.1. Ageing degree and ageing functions

The ageing degree is a bridge parameter between LDPM and HTC models: information concerning the extent of cement and slag hydration are brought from the chemo-diffusion model to the mechanical one, allowing for determining the ageing degree. The latter is computed as follows

$$\dot{\lambda} = \begin{cases} \left(\frac{T_{max}-T}{T_{max}-Tref}\right)^{n_\lambda} (B_\lambda - 2A_\lambda \alpha)\dot{\alpha} & \text{for } \alpha > \alpha_0 \\ 0 & \text{otherwise} \end{cases} \tag{3}$$

in which α is the total reaction degree presented in Eq. (2), α_0 is its value at the end of the setting phase, T_{max} is the maximum temperature at which the hardening is possible under standard condition (≈ 100°C), T_{ref} is the reference temperature for the experimental calibration of the ageing degree. For $T = T_{ref}$, it is $\lambda = 0$ for $\alpha \leq \alpha_0$, and $\lambda = 1$ for $\alpha = \alpha_\infty$. Consequently, one can obtain $B_\lambda = [1 + A_\lambda(\alpha_\infty^2 - \alpha_0^2)/(\alpha_\infty - \alpha_0)]$. The material parameters A_λ and n_λ are calibrated against experimental data.

Then, the ageing degree is exploited to update the mesoscale mechanical properties of the LDPM constitutive laws:

$$E_0 = E_0^{\infty}\lambda; \tag{4}$$

$$\sigma_t = \sigma_t^{\infty}\lambda^{n_a}, \quad \sigma_{c0} = \sigma_{c0}^{\infty}\lambda^{n_a}, \quad r_{st} = r_{st}^{\infty}\lambda^{m_a}; \tag{5}$$

$$l_t = l_t^{\infty}\left[k_a(1-\lambda)+1\right]. \tag{6}$$

E_0, σ_t, σ_{c0}, r_{st}, and l_t are, respectively, the normal modulus, tensile strength, compression strength, shear-to-tensile strength ratio, and the tensile characteristic length at the mesoscale. They are the parameters governing the constitutive laws on which the LDPM formulation relies. The appendix ∞ indicates the asymptotic value of each mechanical property, whose time evolution is a function of the ageing degree and shaped by the material parameters n_a, m_a, and k_a, which must be experimentally calibrated.

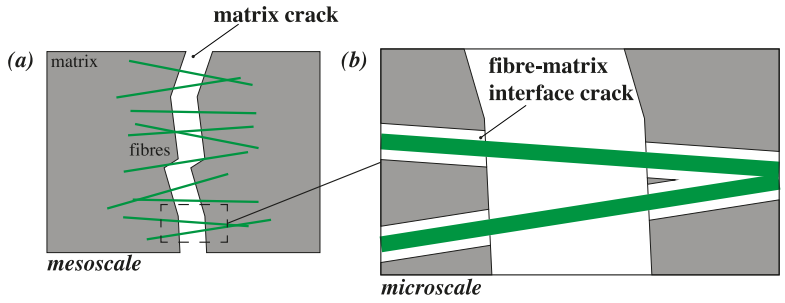

Fig. 3. Numerical model — Two levels in the damage modelling: (a) matrix cracks at the mesoscale; (b) fibre-matrix interface cracks at the microscale.

2.3.2. Effect of crack opening on moisture permeability

The crack opening, intended as a measure of undergone damage, is the second bridging parameter between LDPM and HTC models. The moisture permeability coefficient D_h, introduced in Eq. (1)a, is affected by several factors: (i) pore saturation, (ii) temperature, (iii) ageing, (iii) tortuosity and (iv) connectivity of the pore structure at the microscale [40]. Beyond these aspects, cracking also impairs the ability of concrete to resist to water penetration. Therefore, the moisture permeability coefficient should be defined for uncracked and cracked conditions. As presented by Di Luzio and Cusatis [40,65], D_h in uncracked conditions reads

$$D_h^{uncracked}(h,T) = D_1\left[1+\left(\frac{D_1}{D_0}-1\right)(1-h)^n\right]^{-1}\exp\left(\frac{E_{ad}}{RT_0}-\frac{E_{ad}}{RT}\right) \quad (7)$$

where D_0 and D_1 represent the moisture permeability in complete dry and saturated conditions, respectively, that, with n, are material parameters to be calibrated by best fitting experimental data. T is the actual temperature, T_0 is the reference room temperature, and E_{ad} the diffusion activation energy [67].

For cracked conditions the approach proposed by Di Luzio et al. [5] is adopted, in which the empirical coefficient, $f_D(w_c) \geq 1$, expressing the increase of permeability due to damage and cracking, is introduced.

$$f_D(w_c) = 1+\frac{999e^{n_c}\xi}{1-(1-e^{n_c})\xi} \quad \text{with} \quad \xi = \min\left[\frac{\max(w_c-w_{c0};0)}{w_{c1}-w_{c0}};1\right] \quad (8)$$

Then, D_h in cracked conditions values

$$D_h^{cracked}(h,T,w_c) = f_D(w_c)\cdot D_h^{uncracked}(h,T) \quad (9)$$

The formulation of $f_D(w_c)$ stems from the best fitting of experimental data available in the literature. The exponent n_c governs the shape and slope of $f_D(w_c)$, whereas w_{c0} is the threshold value in correspondence of which D_h starts growing due to damage, and w_{c1} is the crack opening beyond which D_h is assumed not to further increase.

3. Multiscale crack healing model

The modelling approach relies on identifying two different levels of damage: (i) matrix and (ii) fibre-matrix interface cracks. The matrix cracks (Fig. 3a) are induced by either external (i.e., mechanical, geometrical, and environmental loads) and/or internal (e.g., shrinkage restrained deformations) actions and are responsible for the fibres' mechanical activation. The fibre-matrix interface cracks (Fig. 3b) develop during the interface debonding instead and are hereinafter also referred to as *tunnel cracks* between the fibre and the surrounding embedding matrix. They are typically narrower than the matrix cracks, a condition that might imply the expectation of better and faster healing but – at the same time – a more likely shortage of moisture in the vicinity of crack walls due to limited accessibility.

In line with the LDPM discrete approach, the self-healing model deals with matrix and tunnel cracks separately. The autogenous repairing of the former has been presented, together with its calibration and validation for ordinary plain concrete, in [45]. In this work, its implementation at the mesoscale (i.e., in LDPM) has remained unchanged. In contrast, the effect of tunnel cracks healing is taken into account within the calculation of the bridging force carried by the fibre reinforcement. This approach stems from the idea that the recovery of matrix damage and tunnel cracks along the fibre–mortar interface affect the material mechanical behaviour differently. Likewise, the evolution of the moisture-driven healing process at the two observation scales is implemented in the discrete formulation of the HTC model (M-LDPM) separately as well. Although the phenomenon involves the same material at both mesoscopic and microscopic scales, it is convenient to have separate internal variables to characterise their evolution based on dedicated experimental data.

3.1. Healing kinetic law

The healing kinetic law formulated for cementitious materials [5,45] presents no limitations in being used for fibre-reinforced cementitious composites. Following the conceptual differentiation between matrix and tunnel cracks, it can be exploited for capturing both autogenous and eventually stimulated healing. On the other hand, in order to have two separate internal variables feeding the mechanical model at two different levels, in the improved version of M-LDPM, a distinction is made between the normalised healing degree for matrix cracks and that for fibre-matrix interface cracks, $\lambda_{sh}^{(m)}$ and $\lambda_{sh}^{(f)}$ respectively. In the following, the formulation emphasising such distinction is reported, with no theoretical differences with respect to the original one [5,45]. The superscript *(i)* represents a generic index, which can be either *(m)* or *(f)*, depending on which scale one is referring to.

The modelling of the healing process is based on a simple assumption: the phenomenon results from two main contributing factors, namely (i) the delayed hydration of the unreacted cement grains and (ii) the precipitation of calcium carbonate ($CaCO_3$) crystals into the cracks, due to the carbonation reactions between portlandite and carbonate ions or carbon dioxide. Both phenomena are water-driven mechanisms, so the model must consider the strong correlation between the moisture availability in the vicinity and inside the cracks and the process evolution. This aspect is considered in the calculation of the proportional coefficient in the kinetic law, between the healing degree $\lambda_{sh}^{(i)}$ and its rate $\dot{\lambda}_{sh}^{(i)}$. The latter is assumed to be inversely proportional to the healing degree. Hence, it is maximum when the process starts and linearly decreases as the phenomenon evolves. The kinetic law reads

$$\dot{\lambda}_{sh}^{(i)} = \tilde{A}_{sh}^{(i)}\left(1-\lambda_{sh}^{(i)}\right) \quad (10)$$

in which $\tilde{A}_{sh}^{(i)}$, the inverse of the reaction characteristic times, is calculated as

$$\tilde{A}_{sh}^{(i)} = \tilde{A}_{sh0}^{(i)}\cdot f_h(h)^{(i)}\cdot f_w(w_c)^{(i)}\cdot\exp\left[-\frac{E_{sh}^{(i)}}{R}\left(\frac{1}{T}-\frac{1}{T_{ref}}\right)\right] \quad (11)$$

where $f_h(h)^{(i)}$ and $f_w(w_c)^{(i)}$ are the moisture and crack opening coefficients, respectively, $E_{sh}^{(i)}$ the healing activation energy, R the universal

constant for gas, T_{ref} the reference temperature and T that one at which the process occurs. Finally, $\tilde{A}^{(i)}_{sh.0}$ is the inverse of the reaction characteristic times in standard conditions ($RH = 100\%$, $T = T_{ref}$, $w_c = 0$) and values

$$\tilde{A}^{(i)}_{sh0} = \tilde{A}^{(i)}_{sh1}\left(1 - \alpha_c^{sh(i)}\right) c + \tilde{A}^{(i)}_{sh2} \cdot ad \tag{12}$$

with $\tilde{A}^{(i)}_{sh1}$ and $\tilde{A}^{(i)}_{sh2}$ two empirical parameters to calibrate against dedicated experimental data.

The coefficient $f_h(h)^{(i)}$ accounts for the effect of moisture supply on the healing process. It reads

$$f_h(h)^{(i)} = \left[1 + \left(a_h^{(i)} - a_h^{(i)} h\right)^{b_h^{(i)}}\right]^{-1} \tag{13}$$

The superscript *(i)* denotes that $f_h(h)$ might be different between matrix and tunnel cracks. The material parameters a_h and b_h are calibrated or assumed upon experimental evidence at both scales of observation. This enables to capture the different moisture accessibility of matrix and tunnel cracks. The former are usually directly exposed to the external environment; hence easier to be reached by moisture. On the contrary, the tunnel cracks are generally located in the inner part of the element; then, the water is required to overcome tortuous and longer paths to reach the crack walls.

The coefficient $f_w(w_c)^{(i)}$, instead, is in charge of tuning the process rate depending on the width of the crack being healed. It values 0 as long as the crack opening exceeds the threshold value $w_{c0}^{sh(i)}$, which is again differentiated for matrix and tunnel cracks. When $w_c \geq w_{c0}^{sh(i)}$ the coefficient $f_w(w_c)^{(i)}$ evolves with the following law

$$f_w(w_c)^{(i)} = \left[1 + \left(a_w^{(i)} \cdot w_c\right)^{b_w^{(i)}}\right]^{-1} \tag{14}$$

The double degree of freedom allows to properly simulate the effect of crack opening on the process kinetics. The threshold $w_{c0.sh}$, beyond which the healing starts, is set according to the different typical crack width ranges featuring the healing at the meso- and microscale. Whereas for matrix cracks, it can be assumed that to avoid triggering the numerical model for cracks whose dimension is of the same order of magnitude as concrete macroporosity, it is necessary to adopt a smaller threshold for the healing of tunnel cracks. As a matter of fact, the debonding process typically involves tunnel cracks whose width ranges about a few microns.

3.2. Healing effect on fibre bridging force

Single-fibre pull-out tests showed that pull-out strength is affected by the healing of interface cracks. Al-Obaidi et al. [68] presented a study showing that both pull-out energy and bond strength after healing is significantly greater than that one measured on the same pre-damaged specimens without healing products at the fibre-matrix interface. Similarly, Qiu et al. [52] published detected experimental trends going in the same direction. The bond strength, when pre-damaged specimens are exposed to a moist environment, experiences a non-negligible growth, even after short curing periods. As a matter of fact, whenever the healing process happens, it yields delayed hydration products and $CaCO_3$ crystals filling the tunnel crack between the fibre and the surrounding mortar. This results in a recovery of the interface frictional bond.

The phenomenon is implemented in LDPM-F by updating the value of the fibre bridging force $P(v)$, proportional to the matrix–fibre slip v, with a coefficient proportional to $\lambda_{sh}^{(f)}$. The updated constitutive law for the fibre load reads

$$P\left(v, \lambda_{sh}^{(f)}\right) = \left(1 + \gamma_{sh} \cdot \lambda_{sh}^{(f)}\right) P(v) \leq \alpha \cdot P_0 \tag{15}$$

where $P(v)$ is computed through the fibre pull-out model presented in Appendix B, which differentiates the formulation of the fibre bridging force (see Eq. (25),(26)) depending on whether the slip exceeds or not the limit value at full debonding v_d (see Eq. (24)). P_0, instead, represents the bridging force at full debonding (see Eq. (26)). In order to comply with the experimental evidence available so far, on one hand, the coefficient $\left(1 + \gamma_{sh} \cdot \lambda_{sh}^{(f)}\right)$ has been conceived to capture the increase of pull-out energy, detected by Al-Obaidi et al. [68], whereas the kinetic law behind $\lambda_{sh}^{(f)}$ can replicate the faster healing of the tunnel cracks, in line with the results of Qiu et al. [52].

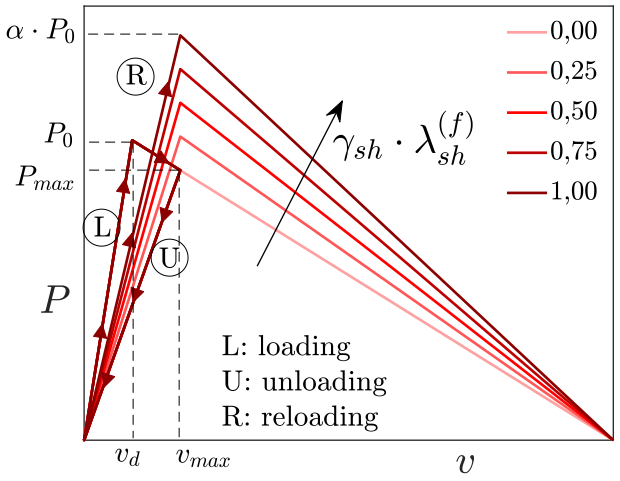

Fig. 4. Numerical model — Effect of healing on the fibre load vs. slip law.

Referring to a single-fibre pull-out test, in Fig. 4, the effect of the tunnel crack self-healing on the mechanical response is qualitatively shown. After the loading and unloading stages (branches L and U), the specimen is exposed to given environmental conditions for some time long enough to permit the self-healing process to develop. The cured specimen is then reloaded (branch R) up to rupture. Due to the recovered frictional bond, the specimen might experience a recovery in stiffness and strength to an extent proportional to (i) the degree of completion of the healing process and (ii) the quality of the healing products. By means of Eq. (15), the mechanical model is updated to be capable of capturing this experimental evidence. In Fig. 4, the updated constitutive law is plotted with reference to increasing self-healing degrees, assuming $\gamma_{sh} = 1$.

The coefficient γ_{sh} governs the impact that the healing of the tunnel cracks has on the fibre contribution to the mechanical equilibrium. With $\gamma_{sh} = 0$, it is possible to capture the crack sealing, whereas if $\gamma_{sh} \geq 0$, the load carried by the fibre is enhanced due to the increased friction along the crack walls. The latter has an upper bound $(\alpha \cdot P_0)$ in which the bridging force at full debonding P_0 is either amplified or reduced by the coefficient α. Both γ_{sh} and α are material parameters that must be calibrated against experimental data. Depending on (i) composition of the cementitious composites, (ii) technique adopted to engineer the process, (iii) fibres nature, (iv) curing conditions, and (v) loading regimes, the healing might allow for recovery either partially or even increasing the fibre load-bearing capacity. The parameter α sets the maximum achievable level of recovery. Once calibrated experimentally, γ_{sh} must comply with the condition for which, in case of complete fulfilment of the tunnel crack:

$$\text{if} \quad \lambda_{sh}^{(f)} = 1.00 \implies \gamma_{sh} \leq \frac{\alpha \cdot P_0}{P(v)} - 1 \tag{16}$$

3.3. Parametric study

In order to investigate whether the healing implementation in LDPM-F leads to the expected macroscopic behaviour (Fig. 4), a direct tension test on an FRC specimen has been simulated to assess how it behaves if, after being damaged, tunnel crack self-healing increases.

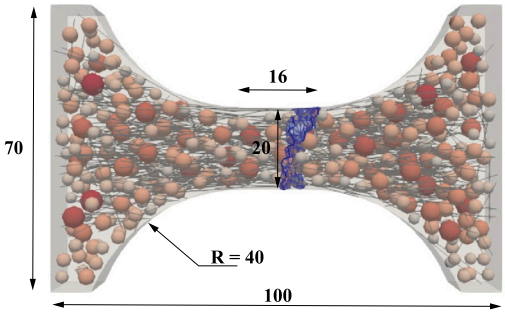

(a) Dogbone FRC specimen: aggregate particles, fibres and cracks.

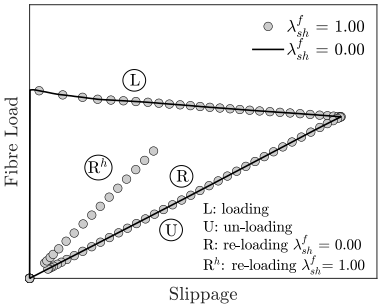

(b) Fibre load vs. slippage curve experienced along one of the most damaged facets.

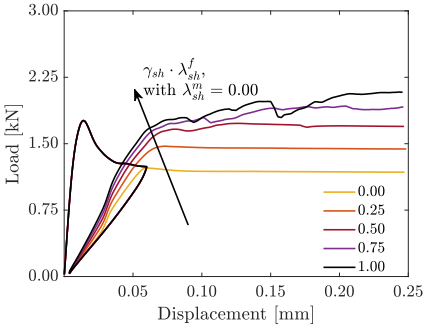

(c) Pure tension for precracking and up to failure with only tunnel cracks healing.

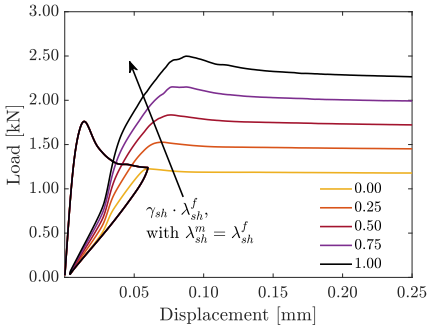

(d) Pure tension for precracking and up to failure with both matrix and tunnel cracks healing.

Fig. 5. Numerical model — Influence of healing implementation on FRC dogbone specimen under uniaxial tension load.

Table 1
Mix composition of the reference fibre-reinforced concrete (dosages in kg/m^3).

Constituent	Content in kg/m^3
cement	600
water	200
aggregates 3-6 mm	1518
steel fibres d_f = 0.22 mm, L_f = 20 mm	0.50% by volume

The concrete composition is reported in Table 1, where it is possible to see that the aggregate size and fibres length comply with the condition: $L_f \geq 3D_{max}$, which ensures that the fibre–aggregate interaction can develop properly [69].

A simple set of numerical simulations has been carried out, employing a dogbone specimen, whose geometry is reported in Fig. 5a. The sample has been loaded in pure axial tension up to featuring a single prominent crack approximately 60 μm wide. Then, it has been completely unloaded. After reaching the zero-load condition, the sample has been reloaded to failure. The reloading stage has been performed by assuming for the tunnel cracks self-healing degree, λ^f_{sh}, increasing fixed values between 0.00 and 1.00. The numerical simulations have been carried out in two different scenarios: (i) with no matrix crack healing, λ^m_{sh} = 0.00, and (ii) in the hypothesis of matrix and tunnel cracks healing evolving identically, $\lambda^m_{sh} = \lambda^f_{sh}$. It has been assumed c_{sh} = 1.00, γ_{sh} = 1.00, and α = 2.00.

Firstly, it is essential to assess how the model performs at the single fibre-facet intersection to see if the P–v curve actually evolves as presented in Fig. 4. The comparison between the fibre load vs. slip curves, referred to one of the most damaged LDPM facets and obtained with λ^f_{sh} equal to zero and 1.00, is shown in Fig. 5b. The effect of healing acts as expected, though the re-loading in the presence of healing stops before reaching the ultimate slip (Fig. 5b). As it stands out from Fig. 5c, the numerical model is able to capture what has been experimentally observed by Qiu et al. [52], who detected a recovery in load-bearing capacity at macroscale with a negligible matrix crack healing. Finally, in Fig. 5d, the model captures the coupled effect on the fracturing behaviour induced by the simultaneous autogenous repairing of both matrix and tunnel cracks.

4. Simulation of UHPC self-healing

The model presented in the previous sections has been used to simulate laboratory tests carried out on a UHDC mix, with the purpose of showcasing the model's capability of capturing (i) the growth in strength and stiffness due to the material ageing, and (ii) the recovery that can be detected in strength and stiffness at the macroscale due to either autogenous and/or stimulated healing at the micro- (tunnel cracks) and mesoscale (matrix cracks). The coupling between ageing and healing models is crucial to avoid overestimating the healing effect on mechanical performance.

Being the model a full coupled model, its calibration requires to proceed step-by-step. Each calibration step relies on the comparison between numerical results and consistent experimental evidence. As first step, it is necessary to identify the parameters governing the ageing model. Afterwards, it is possible to calibrate the self-healing of the matrix cracks, by using test data relevant to the plain material. Finally,

Table 2
Composition of the UHPC mix tested by Lo Monte and Ferrara [70] and Al-Obaidi et al. [71].

Constituent	Content in kg/m^3	Mix proportion by cement content
Cement type I 52.5 R	600.00	1.0000
Slag	500.00	0.8334
tap water	200.00	0.3334
Silica sand (d_{max} = 2.0 mm)	982.00	1.6375
Steel fibres (1.5% by volume)	120.00	0.2000
Superplasticizer (MasterGlenium ACE300)	33.00	0.0550
Crystalline admix. (Penetron ADMIX)	4.80	0.0080

the self-healing of the tunnel cracks can be calibrated by looking for the best fitting with experimental evidence detected on the fibre reinforced material.

4.1. Calibration and validation of the ageing model

Lo Monte and Ferrara [70],Al-Obaidi et al. [71] presented experimental evidence on the flexural and fracturing behaviour of a UHDC mix (Table 2) at two different ages: 90 and 730 days. In this work, the LDPM and HTC parameters governing the simulation of ageing, diffusion, and mechanical behaviour of the plain matrix are inherited from a companion computational activity on the same material [28,72] and are reported in Tables 3 and 4, respectively. Instead, the LDPM parameters for matrix–fibre interaction are calibrated and validated by employing the experimental trends detected by Lo Monte and Ferrara [70],Al-Obaidi et al. [71].

Lo Monte and Ferrara [70] carried out 4-point bending tests on two different specimens: deep (500 × 100 × 100 mm^3) (Fig. 7a) and thin (500 × 100 × 25 mm^3) (Fig. 7b) beams. In addition, the authors presented uniaxial (unconfined) compression tests on 100 mm-side cubes (Fig. 7d). Both flexural and compression tests were performed on 90-day-old specimens, cured in the moist chamber with RH = 90% and T = 20 °C. The thin beams were cast in larger moulds with fresh concrete flowing parallel to the long side to orient the fibres accordingly and have them as much as possible orthogonal to the expected crack openings. Instead, casting the deep beams featured a flow-oriented mix pouring from the top downwards at the centre of the formwork.

As mentioned above, the flexural and fracturing behaviour was also investigated by Al-Obaidi et al. [71]. The authors presented an experimental campaign in which the same material was tested after roughly two years after casting. In the Horizon 2020 ReSHEALience project framework, real structures were designed and built as proof of the UHDC concept. One of these structures is the EGP (Enel Green Power Plant) pilot, a basin for geothermal water collection, serving a geothermal power plant owned and run by the Enel Green Power company in Chiusdino, Italy. The basin was designed and built to have three compartments, each of them realised by employing different materials and building concepts. During the casting of the UHDC-based compartment, extra precast slabs were cast and shipped to Politecnico di Milano (Laboratory for Testing Materials, Buildings, and Structures) to perform mechanical and durability tests. Small beams with dimensions of 500 × 100 × 30 mm^3 (Fig. 6c) were obtained from the precast UHDC elements and employed in 4-point bending tests.

In both mentioned laboratory campaigns, three mixes were analysed: the reference one (Table 2), considered in this work, and two variants whose recipes were enriched with either nano-alumina or nano-cellulose.

The LDPM parameters that govern the matrix–fibre interaction have been calibrated through the best fitting between numerical and experimental curves relevant to the 90-day-old deep beams.

In order to reduce as much as possible the computational time, the numerical simulations have been run on meshes featuring a width smaller than the actual sample size. Then, deep beams were simulated through 25 mm wide mesh, whereas a width of 50 mm was used for the thinner specimens.

In addition, to further limit the number of mesh degrees-of-freedom, the coarse-graining technique, as presented in [73], has been adopted by using a coarse-graining factor $\kappa = 3.0$ [74]. This approach has facilitated the construction of the LDPM mesh considering $d_a = d_{max} =$ 6.0 mm and $d_0 = 3.0$ mm, and $n_F = 0.65$. Further details can be found in [28].

In order to capture the preferential orientation of the fibres into the thin beams, and relying on the results published by Ferrara et al. [75], 50% of them have been oriented parallel to the specimen's longest dimension. By contrast, a full random orientation has been used for deep beams because the casting setup does not justify any assumption about a preferential fibres' orientation. Therefore, the numerical curves hereinafter shown represent the average of six simulations. Six different mesh seeds were used for each simulation to minimise bias from particle placing on model calibration and validation. The numerical curves hereinafter shown are the average of six simulations.

To limit the computational cost, the specimens of the 4-point bending test on deep beams, as shown in Fig. 7, have been modelled through a composite mesh, with the external portions simulated with continuum finite elements and the central part with the discrete elements, where coarse aggregates and steel fibres are explicitly simulated and randomly placed, according to the input generation parameters.

After mesh generation, the 90-day curing and the subsequent mechanical tests have been simulated. At the end of the curing period, the ageing degree λ at each node of the flow lattice system has been interpolated to the nearest facet centroids. Afterward, relying on the asymptotic values of LDPM parameters calibrated for the plain matrix [28], the updated mechanical properties have been derived. The matrix–fibre interaction parameters, instead, have been identified by the best match between numerical and experimental load (nominal strength) vs. COD (Crack Opening Displacement) curves (Fig. 8). The calibrated parameters are reported in Table 5.

The mix was designed to promote strain-hardening in tension by inducing a multi-cracking pattern through the quality (shape and tensile strength) and volume fraction of the steel fibres. The typical cracking patterns detected in deep beams, shown in Fig. 9a, confirm that the material behaved as expected. The numerical model does have the capacity to simulate the development of multiple cracks. At the beginning of the softening branch, namely when COD approaches 2.0 mm, the simulated specimen presents three damage zones for a total of five cracks (Fig. 9b).

In Fig. 10, the cracks resulting from the numerical simulation are shown in more detail. This allows to appreciate how the discrete model enables a refined crack opening calculation along the crack longitudinal axes. This feature is particularly appealing for multi-physics analyses, in which physical properties (e.g., moisture permeability, self-healing reaction affinity) if adequately modelled, might be updated depending on the local crack width, which is hampered to any classical continuum-based approach.

For the compression response, the effect of fibres is expected to be marginal, as confirmed by the numerical results. In Fig. 11, the comparison between the plain [28] and fibre-reinforced composite is shown: the red bold curve refers to the simulation of the compression test on 90-day old UHPC 100 mm cubes, whereas the black dashed one has been obtained by simulating the same test on plain cylinder specimens after a 90-day curing period. Both curves are the averages over six different meshes. In the laboratory campaign, only the average experimental strength was reported [70]. At 90 days, it was found to have a value of 136.85 MPa, whereas the numerical one resulted in 134.12 MPa. For the sake of comparison, relevant to the plain concrete cylinders, the experimental and numerical compression strengths value 129.61 MPa and 129.72 MPa, respectively. The ratios between cylinder and cube strengths are 0.95 for experimental data and 0.97 relevant to numerical results. The registered increase is likely due to the geometry

Table 3
LDPM parameters for the investigated UHPC, calibrated and validate by Cibelli et al. [28].

Group	Parameter	Value	Parameter	Value
elastic	E_0^{∞} (MPa)	70 975	α (–)	0.31
fracturing	σ_t^{∞} (MPa) l_t^{∞} (mm)	13.31 8.47	n_t (–) r_{st}^{∞} (–)	0.001 3.23
compression	σ_{c0}^{∞} (MPa) κ_{c0} (–) κ_{c2} (–)	500.00 2.00 2.00	H_{c0}/E_0 (–) κ_{c1} (–)	0.36 1.00
frictional	σ_{N0}^{∞} (MPa)	350.00	μ_0 (–)	0.50
unloading/reloading	k_c (–) k_s (–)	0.50 0.50	k_t (–)	0.50
ageing	n_a (–) k_a (–)	5.47 74.97	m_a (–)	−3.59

Table 4
HTC parameters for the investigated UHPC, calibrated and validate by Cibelli et al. [28].

Group	Parameter	Value	Parameter	Value
Sorption isotherm	g_1 (–)	1.50	g_2 (–)	0.191
Cement hydration	$A_{c.1}$ (1/h) $E_{a.c}$ (kJ/mol) $\tilde{\alpha}_c^{\infty}$ (–) $\tilde{Q}_c^{\infty}$ (kJ/kg)	8.86×10^6 40.00 0.651 469.45	$A_{c.2}$ (–) η_c (–) ζ_c (–)	0.005 5.124 0.350
Slag reaction	$A_{sl.1}$ (1/h) $E_{a.sl}$ (kJ/mol) $\tilde{\alpha}_{sl}^{\infty}$ (–) $\tilde{Q}_{sl}^{\infty}$ (kJ/kg)	3.28×10^{14} 80.00 0.063 800.00	$A_{sl.2}$ (–) η_{sl} (–) ζ_{sl} (–)	0.05 9.330 0.250
Bound water	κ_c (–)	0.247	κ_{sl} (–)	0.355
Chemical shrink.	κ_{sh} (–)	0.148		
Moisture permeability	D_0/c (mm^2/h) n (–)	1.00×10^{-4} 3.9	D_1/c (mm^2/h) $E_{a.d}$ (kJ/mol)	3.10 22.45

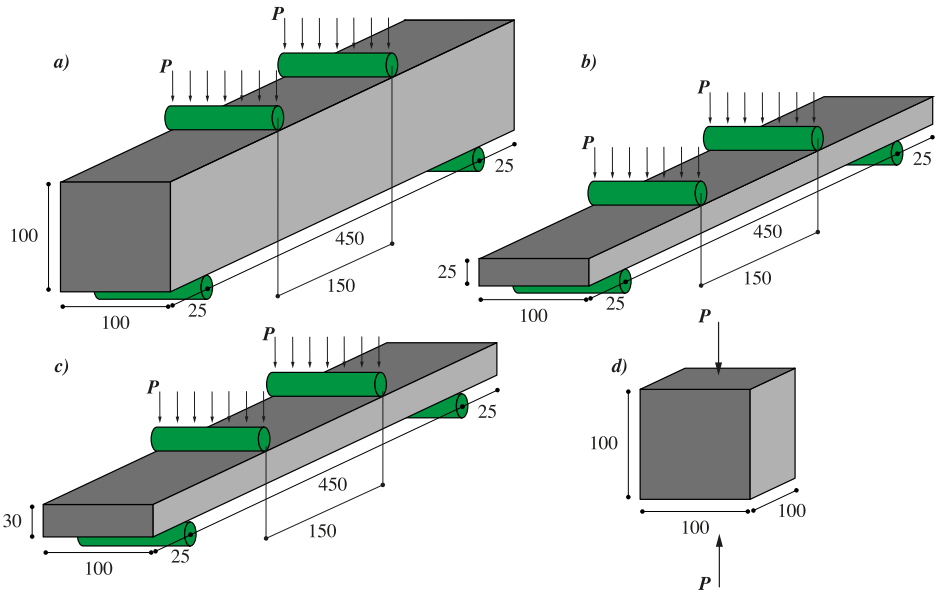

Fig. 6. Numerical simulations – (a) **deep beam** - prismatic specimens with dimensions 500 × 100 × 100 mm^3; (b) **thin beam** - prismatic specimens with dimensions 500 × 100 × 25 mm^3; and (c) **thin beam** - prismatic specimens with dimensions 500 × × 100 × 30 mm^3.

change rather than the presence of fibres in the cube samples. As shown by many authors [76–78], the latter seem to significantly affect the post-peak response, leading to a less steep softening branch.

To complete the picture of the UHPC ageing modelling, the flexural tests on thinner specimens have been simulated by employing the parameters in Table 5. This procedure aims to validate the previously discussed calibration.

Firstly, the 4-point bending test on thin beams has been simulated. The whole sample has been simulated employing an LDPM mesh (Fig. 12), with the same generation settings used for the central

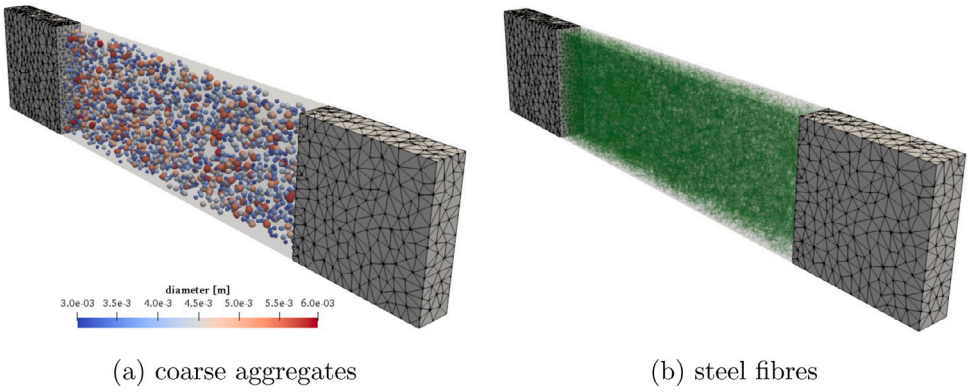

Fig. 7. Numerical simulations — Simulated coarse aggregates and steel fibres within the deep beam mesh.

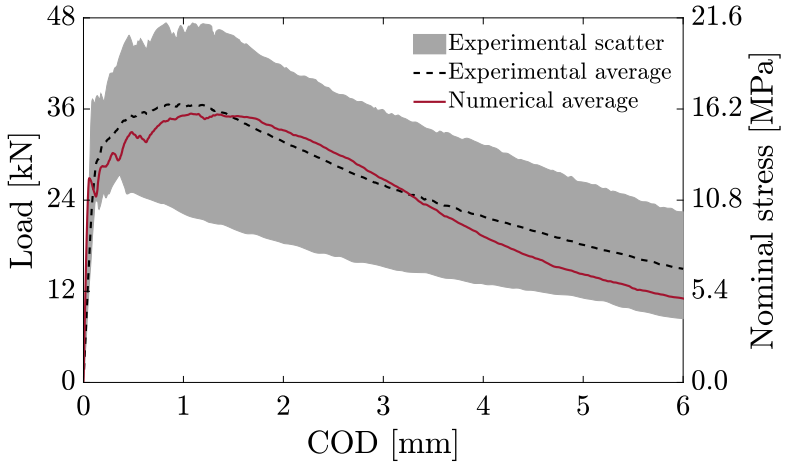

Fig. 8. Calibration — Comparison between experimental and numerical curves for 90-day old deep beams.

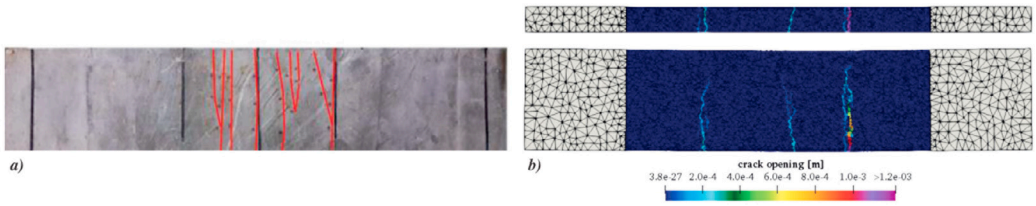

Fig. 9. Calibration — Comparison between typical experimental [70] and numerical crack pattern.

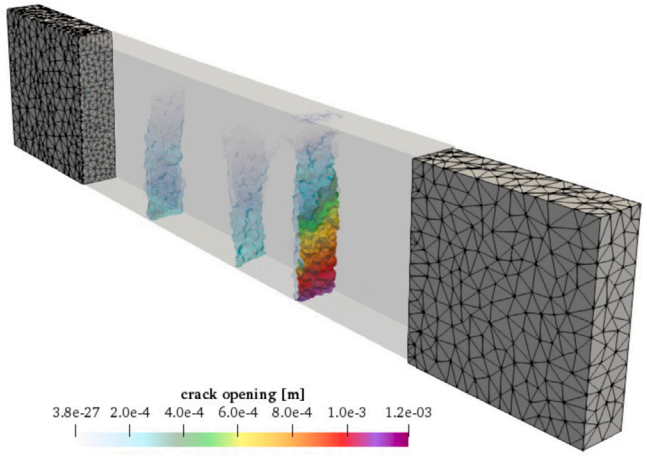

Fig. 10. Calibration — Simulated crack pattern in deep beam specimen.

Table 5
Calibration — LDPM parameters governing the fibre-matrix interaction for the investigated UHPC.

Parameter	Value	Parameter	Value
τ_0 (MPa)	10.12	G_d (N/m)	0.0
β (–)	−0.088	$k_{sp}\sigma_t$ (MPa)	150.00
k_{sn} (–)	0.40	k_{rup} (–)	0.60
γ_p (–)	1.00		

part of the deep beams. In this case, as discussed above, because of the casting procedure, the fibres have been inserted by imposing a preferential orientation so that 50% of the fibres are parallel to the element's longitudinal axis. The computational time has been reduced by employing a mesh with reduced width, namely 50 mm instead of 100 mm.

The experimental and numerical load (nominal stress) vs. COD curves are plotted for comparison in Fig. 13. Looking at the experimental and numerical averages, the model seems to accurately catch

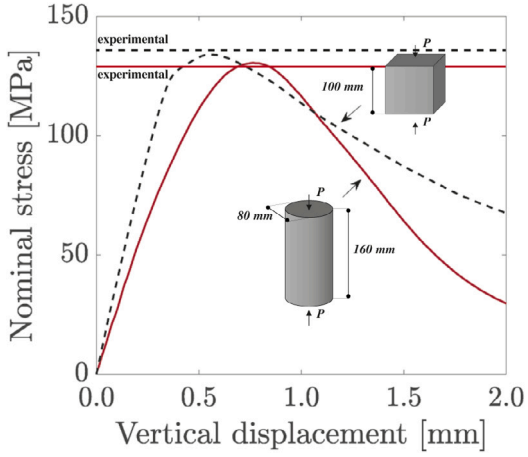

Fig. 11. Validation I — Comparison between experimental and numerical curves after 90 days from casting, for the plain matrix and the fibre-reinforced composite.

Table 6
Healing model— The calibrated values of the parameters governing the healing of the matrix cracks [79].

Parameter	Value	Parameter	Value
$E_{sh}^{(m)}$ (kJ/mol)	41.60	$\tilde{A}_{sh1}^{(m)}$ (m^3/kg h)	8.5 x10^{-6}
$\tilde{A}_{sh2}^{(m)}$ (m^3/kg h)	7.5 × 10^{-6}	$w_{c0.sh}^{(m)}$ (mm)	0.005

the material response. As a matter of fact, the numerical curve fits the experimental average. This result confirms that the model is capable of capturing changes in material response for different geometries.

It is interesting to see that the simulated crack pattern for thin beams features a larger number of relevant cracks than those observed for deep beams. This difference coincides with what was observed in the laboratory. Then, it is possible to state that the model captures not only the fracturing strength for different geometries, i.e., structural behaviour, but also the fracture process, i.e., failure mode. Concerning the former, the average experimental values change from 16.2 MPa to 24.6 MPa for deep and thin beams, respectively. The numerical peak, instead, moves from 16.0 MPa to 29.1 MPa. Fig. 14 compares experimental and numerical crack patterns, showing that the multi-cracking process and failure mode are well captured.

In Fig. 15, it is possible to have a clearer idea of the smeared damage occurring along the tested specimen. Non-negligible damage occurs at the support and load pins due to the numerical strategy adopted to impose the kinematic and static boundary conditions. However, this does not play any role in the simulation of the element response.

The last set of numerical analyses has been run to simulate the 4-point bending tests on 2-year-old specimens, having a geometry similar to the thin beams, which differ only in thickness: 30 mm instead of 25 mm. The available data did not include evidence of the crack pattern. However, due to the marginal geometrical difference between the two sample groups, it can be reasonably assumed that the crack patterns develop similarly. In the following, the comparison between numerical and experimental load (nominal stress) vs. COD curves is shown (Fig. 16). The model captures the material response with a sufficient level of accuracy, confirming its predictive capacity once calibrated.

4.2. Calibration and validation of the self-healing model

The calibration of the parameters governing the healing kinetic law in M-LDPM has been presented in a recent article [79], where the effect of matrix cracks sealing on the chloride penetration was simulated. They are reported in Table 6.

It is worth highlighting that the moisture permeability is assumed to be affected exclusively by the closure of matrix cracks. In the model, this aspect is taken into account straightforwardly in the factor governing the crack size dependence of water permeability $f_D(w_c)$ by replacing the crack opening w_c with $w_c \cdot (1 - \lambda_{sh}^{(m)})$. It means that the actual damage affecting the moisture permeability is reduced proportionally to the evolution of the self-healing process up to completion, i.e., $w_c \cdot (1 - \lambda_{sh}^{(m)}) = 0$ for $\lambda_{sh}^{(m)} = 1$. Hence $\lambda_{sh}^{(m)}$ assumes the meaning of *matrix crack closure degree*.

Table 7
Healing model— The values adopted for the parameters governing the healing of the tunnel cracks.

Parameter	Value	Parameter	Value
$E_{sh}^{(f)}$ (kJ/mol)	41.60	$\tilde{A}_{sh1}^{(f)}$ (m^3/kg h)	1.0 × 10^{-5}
$\tilde{A}_{sh2}^{(f)}$ (m^3/kg h)	1.5 × 10^{-5}	$w_{c0.sh}^{(f)}$ (mm)	0.001

Due to the lack of direct investigation for tunnel cracks, the parameters for the healing kinetic law have been assumed based on the experimental evidence published by Qiu et al. [52]. Since the cementitious material is the same, the process activation energy at the micro-scale, $E_{sh}^{(f)}$, has been assumed to be equal to the value calibrated for matrix cracks. In order to have a faster process, the material parameters $\tilde{A}_{sh1}^{(f)}$ and $\tilde{A}_{sh2}^{(f)}$, steering the effect of un-hydrated cement and additives, have been assumed to be roughly 1.5 times higher then the values adopted at the mesoscale. Finally, since the crack opening at the interface is typically smaller than matrix cracks (about ten μm at full debonding [52]), $w_{c0.sh}^{(f)}$ has been assumed to be five times smaller than $w_{c0.sh}^{(m)}$. Consequently, the interface's healing model is also triggered on those facets experiencing a lower crack opening. The parameters are reported in Table 7.

4.2.1. Matrix cracks

The model's capacity to capture the experimental evidence must be assessed on two different levels: (i) crack closure, and (ii) stiffness and strength recovery of the healed material. As mentioned, the healing-induced crack closure, investigated by Al-Obaidi et al. [80], has been used to calibrate the parameters in Table 6. The mechanical performance of the healed material, instead, has been tested by performing a 3-point bending test on notched prisms, whose dimensions are 160 × 40 × 40 mm^3, with the notch 5 × 5 mm^2. The 45-day-old specimens were first damaged in bending to have a residual crack opening of about 50 μm at complete unloading (Fig. 17b). Then, they were cured in different environments, namely in the moist chamber at 90% relative humidity (exposure A, Fig. 17c) and immersed in distilled water (exposure DW1, Fig. 17d). The effect of the latter condition was additionally investigated in the case of monthly water regeneration (exposure DW2). Afterward, the cured specimens underwent a 3-point bending test up to rupture after 30, 60, and 90 days of curing (Fig. 17e).

The whole experimental program has been simulated in order to calibrate, first, and then validate the healing implementation for matrix cracks. The parameter c_{sh} has been calibrated with reference to the laboratory evidence collected for 30 and 180-day-old healing, whereas the experimental data relevant to 90-day healing have been used for the validation.

In Fig. 18, the results of the calibration stage are presented. The latter were obtained using $c_{sh} = 0.75$. The bold red curves represent the numerical averages, whereas the dashed black lines are the average pre-cracking experimental curves. The re-cracking experimental data are shown with various coloured markers, such as circles, squares, triangles with different orientations, and diamonds.

Since the model cannot capture the effect of distilled water nor monthly regeneration on the material ageing and self-healing, all the laboratory data relevant to the DW1 and DW2 exposure conditions are collected into the group DW, for which saturated boundary conditions of curing have been employed.

The comparison between numerical and experimental curves allows us to formulate some considerations. Numerical and experimental curves agree, confirming the model's capacity to simulate material

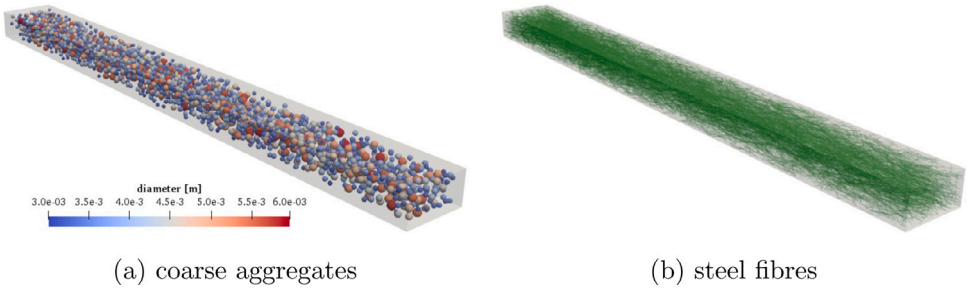

Fig. 12. Numerical simulations — Simulated coarse aggregates and steel fibres within the 25 mm-thick mesh.

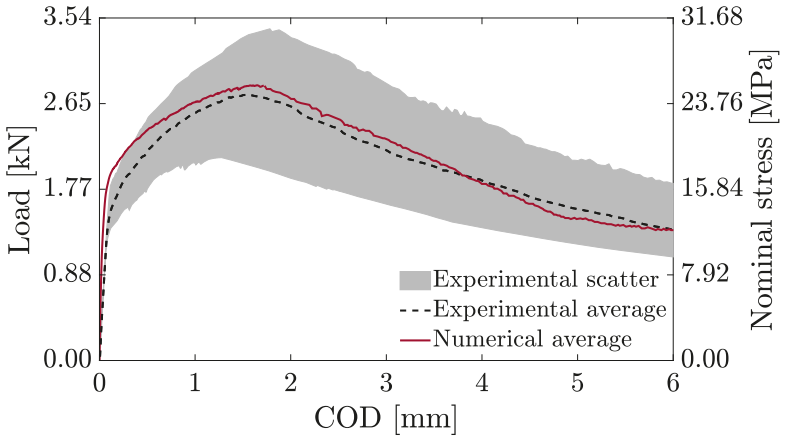

Fig. 13. Validation II — Comparison between experimental and numerical curves after 90 days from casting for 25 mm-thick beams.

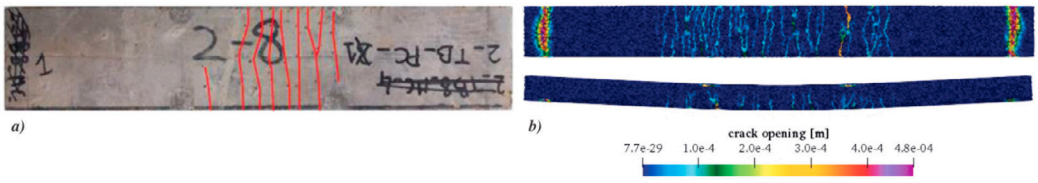

Fig. 14. Validation II — Comparison between typical experimental [70] and numerical crack pattern.

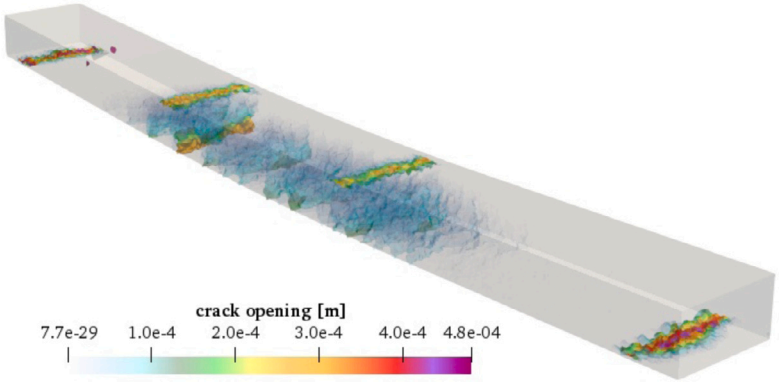

Fig. 15. Validation II — Simulated crack pattern in 25 mm-deep beams.

ageing. It is important to note that the pre-cracking was conducted on samples that were 45-day-old, which is older than the samples used to calibrate and validate the ageing model.

Concerning the re-cracking of the healed material, the match with laboratory measurements appears excellent for exposure condition A (moist chamber). In contrast, the model shows some limits for immersion in distilled water (condition DW). In particular, the model does not fully capture the recovery in stiffness, especially for the 180-day curing period. However, the recovery in strength is still acceptable, in line with what is observed for condition A. The aspects highlighted above are confirmed by the validation results, shown in Fig. 19.

In conclusion, the comparisons of numerical vs. experimental in Figs. 18 and 19 confirm the healing model capacity of capturing the experimental trends. The healing mechanical impact coefficient c_{sh} plays

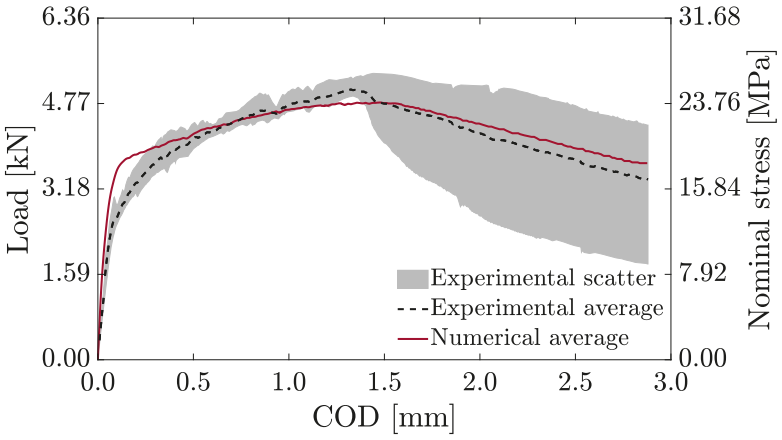

Fig. 16. Validation III — Comparison between experimental and numerical curves after 2 years from casting for 30 mm-thick beams.

Fig. 17. Healing of matrix cracks — Experimental investigation (a) casting, (b) pre-cracking after 45 days in moist chamber, (c) curing with exposure conditions A, (d) curing with exposure conditions DW1 and DW2, (e) broken healed samples after 3-point bending tests.

a crucial role because it permits calibrating the transition from matrix crack sealing [79] to mechanical healing. In Fig. 20 an example of the numerical results is shown in terms of crack opening and self-healing degree.

4.2.2. Tunnel cracks

The self-healing capacity of the UHDC at issue was investigated via a multi-test/multi-parameter approach [20].

The healing assessment was performed through 4-point bending tests on deep ($500 \times 100 \times 100$ mm^3) and thin ($500 \times 100 \times 25$ mm^3) beams, the same geometries employed for the mechanical characterisation by Lo Monte and Ferrara [70] (Figs. 6a,b). The flexural tests were conducted to investigate crack-sealing and mechanical recovery induced by autogenous healing. The experimental program consisted of (i) 60-day curing (RH = 90% and T = 20 °C) after casting, (ii) pre-cracking through 4PBT up to the prescribed residual deformation at the bottom side of 1‰(measured after unloading), (iii) identification and recording of all the detectable cracks via a digital microscope, (iv) 1-month curing in saturated condition (T = 20 °C), (v) recording of all the cracks to measure the degree of sealing, and (vi) re-cracking through 4PBT up to a residual crack opening equal to that gained at the end of the pre-cracking. Steps (v) and (vi) were repeated after 3 and 6 months from pre-cracking. At six months, the specimens were tested up to failure.

The implementation has been tested by simulating the reference experimental campaign. The numerical and experimental results have been compared in terms of mechanical recovery of 4-point bending curves. The numerical results – obtained by employing the parameters reported in Tables 6 and 7 – refer to the simulation of the first precracking–curing–recracking cycle on deep beams specimens carried out in the laboratory, in which the curing period lasted one month. The parameters γ_{sh} and α_{sh} have been assumed equal to 1.00 and 2.00, respectively. As presented by Lo Monte and Ferrara [20], at the end of the pre-cracking stage, the detected crack patterns included one/two major cracks ($w \geq 40$ μm) and a variable ($4 \div 9$) number of minor fractures for all the tested specimens (10 μm $\leq w \leq 40$ μm). As a general trend, the crack sealing degree is higher for wider cracks: it ranges between 0.80 and 1.00 when the crack width is larger than 40 μm, whereas it is included in the interval $0.50 \div 0.80$ when it is derived for the minor cracks. Not all the cracks detected in the laboratory develop throughout the specimen width; in some cases, they involve the sample's bottom face only partially. The numerical results (Fig. 21) show that after unloading, the model simulates two major cracks, whose widths are roughly equal to 130 μm and 80 μm, respectively. The model fails to capture the development of minor cracks during pre-cracking. In terms of crack closure, the Index of Crack Sealing (ICS) in Eq. (17), is compared to the matrix crack self-healing degree, $\lambda_{sh}^{(m)}$. The latter is calculated at each node of the flow lattice system across the crack; hence, its spatial average value must be considered, similar to what was executed within the experimental procedure.

The experimental ICS, instead, is computed as

$$ICS_0 = \frac{A_{F.0} - A_{F.i}}{A_{F.0}} \tag{17a}$$

$$ICS_{i-1} = \frac{A_{F.i-1} - A_{F.i}}{A_{F.i-1}} \tag{17b}$$

where $A_{F.0}$ is the crack area just after pre-cracking, $A_{F.i-1}$ is the crack area just after re-cracking and $A_{F.i}$ is the crack area at the end of the healing period. Thus, it refers to the closure of the crack in the shallower part rather than the complete restoration of the original conditions along the entire crack surface.

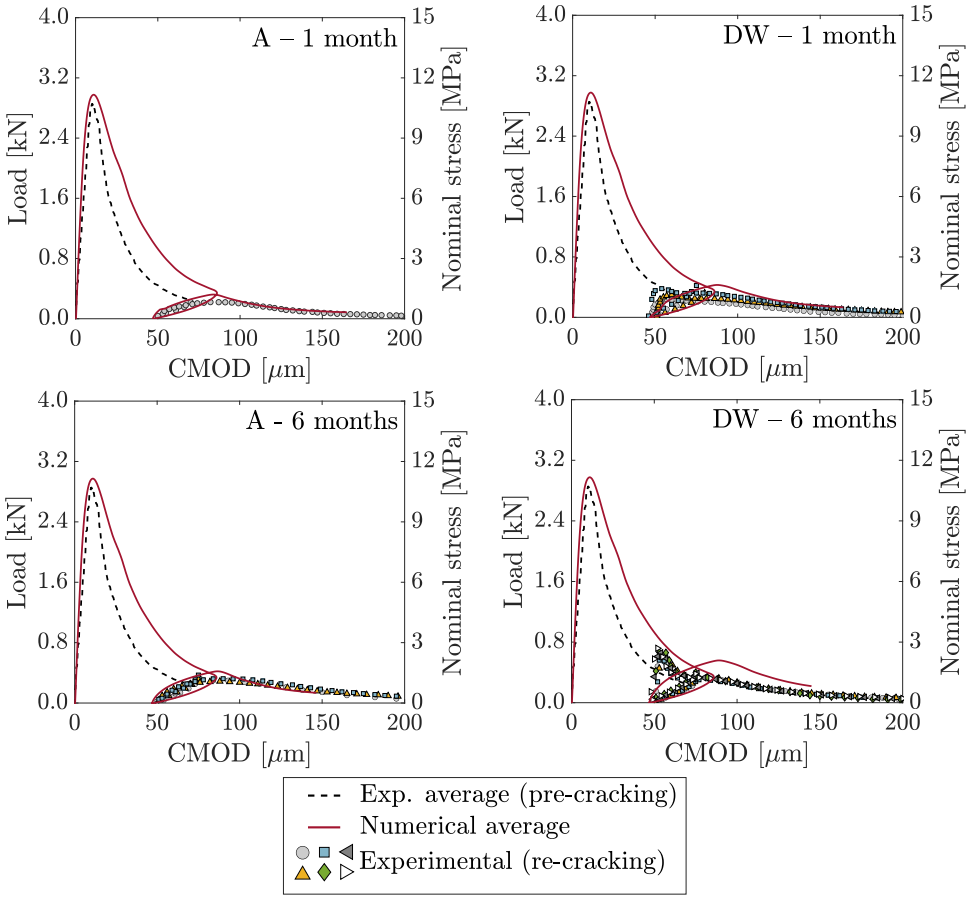

Fig. 18. Healing of matrix cracks — Calibration Comparison between numerical and experimental results for both exposure conditions ((A) moist chamber and (DW) distilled water immersion) after 30 and 180 days.

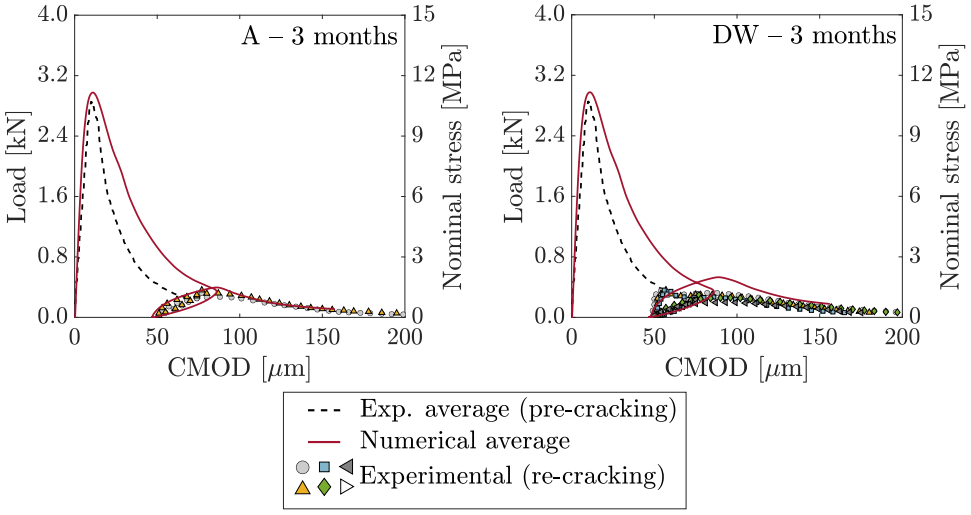

Fig. 19. Healing of matrix cracks – Validation Comparison between numerical and experimental results for both exposure conditions after 90 days.

Experimental ICS ranges between 0.41 and 1.00. In particular, it is approximately 1.00 for the minor cracks, whereas it varies between 0.50 and 0.90 for the major ones.

The numerical results in Fig. 21 refer to one of the six meshes analysed, assumed to be representative of the average simulated behaviour. Focusing on the cracks tip, $\lambda_{sh}^{(m)} = 0.71$ for the 130 μm wide crack, whereas $\lambda_{sh}^{(m)} = 0.62$ for the 80 μm wide crack. The model underestimates the crack closure phenomenon. However, an accurate comparison between the outcomes gained through the numerical implementation and the experimental evidence cannot be performed because the model, relevant to the pre-cracking stage, does not simulate the minor cracks' formation. This might be due to the aggregate coarsening, operated within the mesh generation procedure in order to tackle the computational time. The use of coarser aggregates seems to determine

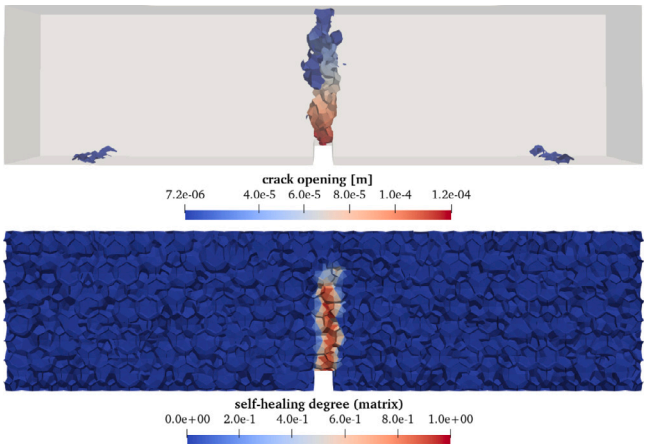

Fig. 20. Healing of matrix cracks – Numerical results for specimen exposed to saturated conditions for 6 months.

a more brittle response and a higher damage localisation. An accurate calibration and validation of the matrix crack self-healing model is presented in [79].

The greater damage localisation featuring the numerical results also affects the comparison between simulation and test outcomes in terms of mechanical recovery. The average numerical curve presents a lower unloading stiffness as shown in Fig. 22. This aspect, along with the LDPM damage-type formulation of the constitutive laws, determines the need to lengthen the loading stage in order to have a residual COD at the full unloading complying with the experimental one. The reloading branch, whose slope is affected by both matrix and tunnel cracks self-healing degrees, does not match the experimental behaviour, and the stiffness recovery results lower than that measured in the laboratory. Instead, the model seems to perform better in terms of strength recovery. This might be probably due to the fact that the model – as it is conceived – does not simulate an actual healing-induced damage reduction, but the beneficial effect acts on the strength level instead for both matrix (i.e., tensile strength) and tunnel (i.e., fibre bridging force) cracks. The local behaviour is affecting the stiffness more with respect to the strength in the damaged/cracked states.

5. Conclusions

A comprehensive model that can simulate in a fully coupled fashion the ageing of materials, the impact of damage on permeability, and the autogenous and/or stimulated healing of cracks was missing in the literature for ordinary and fibre-reinforced cementitious composites. The research activity presented in this article aims to provide a starting point. Specifically for fibre-reinforced concrete, a dedicated numerical approach has been developed to simulate, in addition to the above mention phenomena, the effect of the healing products on the fibre-matrix interaction.

Based on the considerations, assumptions, and results shown and discussed in this manuscript, the following conclusions can be drawn.

- The improved M-LDPM is able to replicate the experimental evidence observed in the reference laboratory campaigns. The model has shown the capability of accurately capturing material ageing. Not only the evolution of the compression and fracture strengths (i.e., structural behaviour) is well simulated, but also the failure mode changes with time and specimen geometry.
- The mechanical model for the matrix crack healing can reliably reproduce the experimental evidence. Once the governing parameters are calibrated, a good agreement is obtained among numerical and test outcomes. This may suggest that the modelling strategy, though relying on a strength limit expansion rather than an actual recovery in terms of deformation, manages to describe the overall mechanical response of the healed specimens in terms of both stiffness and load-bearing capacity.
- The healing model extension for fibre-reinforced concrete has been implemented by enlarging the microscale fibre load-bearing capacity proportionally to the product $\gamma_{sh} \cdot \lambda_{sh}^{(f)}$. The parameter γ_{sh}, similar to c_{sh}, allows uncoupling of the crack sealing and enhancing the fibre-tunnel crack walls friction induced by the healing products. For the tunnel crack healing, only the implementation has been tested on the macroscale, whereas the validation against experimental results is still an open issue, requiring dedicated (and quite demanding) experimental campaigns aimed at assessing the effects of healing on fibre matrix bond through single fibre pull-out tests performed in multiple stages (i.e., pre-slip, healing, pull-out).
- The calibration and validation of the self-healing model for fibre-reinforced concrete need to be further investigated, including an appropriate calibration of the fibre-slip relationship for the simulation of loading–unloading–reloading cycles. To the best of the authors' knowledge, the effect of the tunnel crack self-healing might be improved and validated by simulating single pull-out tests on damaged and healed material, which are still missing in the literature. The calibration by matching a single fibre's behaviour could improve the model's capacity to predict the behaviour at the macroscale.

As a whole, the proposed numerical approach is a promising starting point toward the aim of simulating how the mechanical response of advanced cementitious materials is affected by the autogenous repair of the cracks.

CRediT authorship contribution statement

Antonio Cibelli: Formal analysis, Investigation, Software, Visualization, Writing – original draft, Writing – review & editing. **Liberato Ferrara:** Conceptualization, Project administration, Supervision. **Giovanni Di Luzio:** Conceptualization, Methodology, Supervision, Writing – review & editing.

Declaration of competing interest

The authors declare that they have no known competing financial interests or personal relationships that could have appeared to influence the work reported in this paper.

Data availability

Data will be made available on request.

Acknowledgements

The work described in this paper has been performed in the framework of the project ReSHEALience — Rethinking coastal defence and green-energy Service infrastructures through enHancEd-durAbiLity high-performance cement-based materials, whose funding the authors gratefully acknowledge. This project has received funding from the European Union Horizon 2020 research and innovation program under grant agreement No 760824. The information and views set out in this publication do not necessarily reflect the official opinion of the European Commission. Neither the European Union institutions and bodies nor any person acting on their behalf, may be held responsible for the use which may be made of the information contained therein. The numerical analyses have been performed by means of MARS, an explicit dynamic code distributed by ES3 Inc. (Engineering and Software System Solutions), which is gratefully acknowledged.

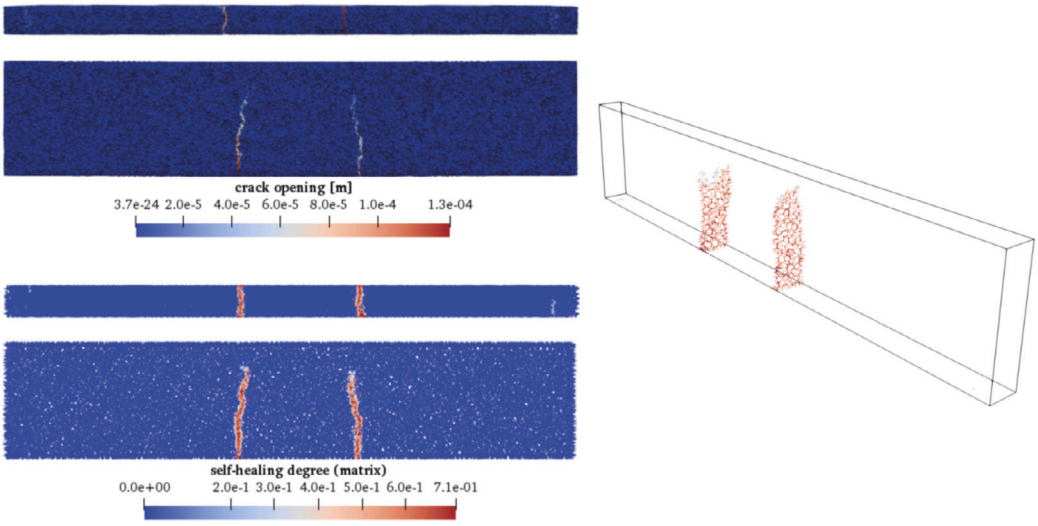

Fig. 21. Crack closure – numerical results.

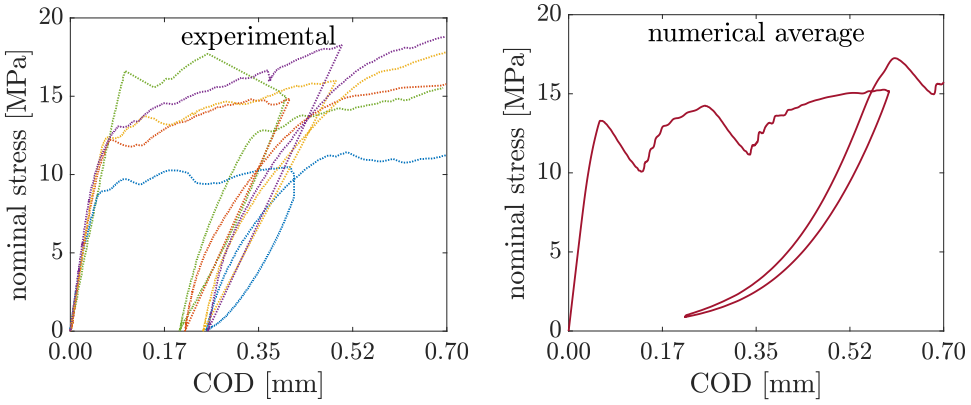

Fig. 22. Mechanical recovery — numerical results.

Appendix A. Damage-type constitutive laws in LDPM

Fracturing behaviour. When the material is subjected to tensile loading ($\varepsilon > 0$), the effective strain and stress permit to define the following relationships in the local reference systems: $\sigma_N = \varepsilon_N(\sigma/\varepsilon)$, $\sigma_L = \alpha\varepsilon_L(\sigma/\varepsilon)$, and $\sigma_M = \alpha\varepsilon_M(\sigma/\varepsilon)$, in which σ is incrementally elastic ($\dot{\sigma} = E_0\dot{\varepsilon}$) and must satisfy the inequality $0 \le \sigma \le \sigma_{bt}(\varepsilon, \omega)$ being $\sigma_{bt}(\varepsilon, \omega)$ a yield surface enforced by means of a vertical (at constant strain) return algorithm. The strain-dependent limit can be expressed as

$$\sigma_{bt}(\varepsilon, \omega) = \sigma_0(\omega)\exp\left[-H_0(\omega)\frac{\langle\varepsilon_{max} - \varepsilon_0\rangle}{\sigma_0(\omega)}\right] \tag{18}$$

where the brackets $\langle\cdot\rangle$ are used in Macaulay sense: $\langle x\rangle = \max\{x, 0\}$, and H_0 is the post-peak softening modulus, whose formulation permits to smoothly pass from a softening behaviour under pure tensile stress ($H_0(\omega = \pi/2) = H_t$) to a perfectly plastic response under pure shear ($H_0(0) = 0$). As a matter of fact, $H_0(\omega) = H_t(2\omega/\pi)^{n_t}$, with n_t softening exponent. In Eq. (18), ω is the parameter representing the degree of interaction between shear and normal loading. Finally, $\sigma_0(\omega)$ is the strength limit for the effective stress and is formulated as

$$\sigma_0(\omega) = \sigma_t\frac{-\sin(\omega) + \sqrt{\sin^2(\omega) + 4\alpha\cos^2(\omega)/r_{st}^2}}{2\alpha\cos^2(\omega)/r_{st}^2} \tag{19}$$

in which $r_{st} = \sigma_s/\sigma_t$ is the ratio between the shear strength, σ_s (cohesion), and the tensile strength, σ_t.

Pore collapse and material compaction. In presence of compression load ($\varepsilon_N < 0$), the normal stress at each facet centroids must satisfy the inequality: $-\sigma_{bc}(\varepsilon_D, \varepsilon_V) \le \sigma_N \le 0$.

$$-\sigma_{bc}(\varepsilon_D, \varepsilon_V) \le \sigma_N \le 0 \tag{20}$$

As for the response under tension and tension/shear, the concrete response is governed by a strain-dependent boundary σ_{bc}, depending on volumetric and deviatoric deformations: ε_V and $\varepsilon_D = \varepsilon_N - \varepsilon_V$, respectively. Determined from the tetrahedra volume variation, the volumetric strain is defined as $\varepsilon_V = (V - V_0)/V_0$, and assumed equals for all the facets belonging the same tetrahedron.

Concrete under compression beyond its elastic limit experiences the early collapse of micro and mesoscale pores, followed by significant material compaction upon contact with collapsed pore walls. LDPM models the inelastic evolution of the boundary under compression in two steps. Firstly, the stress σ_{bc} increases linearly during pore collapse until the compaction strain ($\varepsilon_{DV} = \varepsilon_V + \beta\varepsilon_D$) threshold is reached. Secondly, an exponential evolution captures the effect of densification (rehardening). The formulation reads

$$\sigma_{bc}(\varepsilon_D, \varepsilon_V) = \begin{cases} \sigma_{c0} & \text{for } -\varepsilon_{DV} \le 0 \\ \sigma_{c0} + \langle -\varepsilon_{DV} - \varepsilon_{c0}\rangle H_c(r_{DV}) & \text{for } 0 \le -\varepsilon_{DV} \le \varepsilon_{c1} \\ \sigma_{c1}(r_{DV})\exp[(-\varepsilon_{DV} - \varepsilon_{c1})H_c(r_{DV})/\sigma_{c1}(r_{DV})] & \text{otherwise} \end{cases} \tag{21}$$

where σ_{c0} and ε_{c0} are the stress and strain, respectively, at the onset of pore collapse, r_{DV} is the deviatoric-to-volumetric strain ratio $\varepsilon_D/\varepsilon_V$,

and $H_c(r_{DV})$ the initial hardening modulus. Finally, σ_{c1} and ε_{c1} are the stress and strain when rehardening begins.

In the model, within the boundaries identified in the inequality (20), the normal stress is assumed to be incrementally elastic: $\dot{\sigma}_N = E_{Nc}\dot{\varepsilon}_N$. In order to describe the increased stiffness during unloading, E_{Nc} is defined as

$$E_{Nc} = \begin{cases} E_0 & \text{for } -\sigma_N < \sigma_{c0} \\ E_d & \text{otherwise} \end{cases} \tag{22}$$

where E_d is the densified normal modulus.

Frictional behaviour. In the presence of compression stresses, the shear strength increases due to frictional effects. This phenomenon is modelled through classical incremental plasticity: incremental shear stresses can be calculated as $\dot{\sigma}_L = E_T(\dot{\varepsilon}_L - \dot{\varepsilon}_L^P)$, and $\dot{\sigma}_M = E_T(\dot{\varepsilon}_M - \dot{\varepsilon}_M^P)$, where the plastic strain increments are assumed to obey the normality rule, namely $\dot{\varepsilon}_L = \dot{\lambda}\partial\varphi/\partial\sigma_L$ and $\dot{\varepsilon}_M = \dot{\lambda}\partial\varphi/\partial\sigma_M$. Here, the plastic potential is expressed as $\varphi = \sqrt{\sigma_L^2 + \sigma_M^2} - \sigma_{bs}(\sigma_N)$, in which the functional relationship between shear strength and acting compression stress is captured by the boundary

$$\sigma_{bs}(\sigma_N) = \sigma_s + (\mu_0 - \mu_\infty)\sigma_{N0}\mu_\infty\sigma_N - (\mu_0 - \mu_\infty)\sigma_{N0}\exp\left(\sigma_N/\sigma_{N0}\right) \tag{23}$$

where σ_s is the cohesion, μ_0 and μ_∞ are the initial and final internal friction coefficients, and σ_{N0} is the normal stress at which the transition from μ_0 to μ_∞ happens. Finally, the loading–unloading conditions are expressed by means of the classical Kuhn–Tucker's conditions: $\varphi\dot{\lambda} \le 0$ and $\dot{\lambda} \ge 0$.

Details about the model formulation can be found in Cusatis et al. [57].

Appendix B. Fibre bridging force in LDPM

Model hypotheses.

Model hypotheses are (i) fibres have a negligible contribution to equilibrium during compression stress or stress below the elastic limit, namely $\boldsymbol{P}_f \approx \boldsymbol{0}$ for both $\varepsilon < 0$ and $\boldsymbol{w} = \boldsymbol{0}$; (ii) adjacent fibres and mesoscale cracks have negligible effects on individual fibres. and (iii) each fibre is assumed to be straight, elastic, with negligible bending stiffness, and non-circular cross sections are simulated through an equivalent diameter, calculated as $d_f = 2(A_f/\pi)^{1/2}$ with A_f fibre cross-sectional area.

Fibre pull-out model. Fully debonded fibre results in a purely frictional mechanism. According to Lin et al. [81], in LDPM-F, v_d slip at full debonding is calculated as follows

$$v_d = \frac{2\tau_0 L_e^2}{E_f d_f} + \left(\frac{8G_d L_e^2}{E_f d_f}\right)^{1/2} \tag{24}$$

in which L_e is the embedment length and E_f the modulus of elasticity of the fibre. In Eq. (24), τ_0 and G_d are the constant value of frictional stress for the portion of the embedded fibre that has debonded and the bond fracture energy, respectively. They are two parameters which govern the debonding stage, modelled as a tunnel-type cracking process [82].

During the debonding stage ($v < v_d$), the fibre bridging force is given as Lin et al. [81]

$$P(v) = \left[\frac{\pi^2 E_f d_f^3}{2}\left(\tau_0 v + G_d\right)\right]^{1/2} \tag{25}$$

After full debonding ($v > v_d$), the mechanism is entirely frictional and the fibre load results from Lin et al. [81]

$$P(v) = P_0\left(1 - \frac{v - v_d}{L_e}\right)\left[1 + \frac{\beta\left(v - v_d\right)}{d_f}\right] \tag{26}$$

where $P_0 = \pi L_e d_f \tau_0$, whereas β is the coefficient in charge of shaping the relationship to capture the high variability of the frictional interface nature Lin and Li [83]. When the friction at the interface does not depend on the slip, β is set to zero. In case of either slip hardening or slip softening friction, it assumes positive ($\beta > 0$) or negative ($\beta < 0$) values, respectively.

Micromechanics at matrix–fibre interface. The orientations of the embedded and free (where the cracking–bridging force is acting) fibre portions are different. At the point where the fibre exits the matrix and changes orientation, bearing stresses appear in the underlying matrix. When this localised stress field reaches a sufficient intensity, spalling occurs, and the embedment length of the fibre is consequently reduced by a length s_f. The force in the bridging segment experiences a sudden drop, and also the deflection angle between the two fibre segments changes from φ_f to φ_s'. Denoting the angle between the embedded fibre direction ($\boldsymbol{n}_f$) and facet normal orientation ($\boldsymbol{n}$) as $\vartheta = \arccos\left(\boldsymbol{n}_f^T\boldsymbol{n}\right)$, a reasonable estimate of the spalling length is obtained by the following expression

$$s_f = \frac{P_{f.N}\sin(\vartheta/2)}{\sigma_{sp} d_f \cos^2(\vartheta/2)} \tag{27}$$

in which $P_{f.N}$ is the normal component of the total force P_f carried by the fibre, and σ_{sp} represents the matrix strength against spalling, related to the mesoscopic tensile strength (σ_t).

Where the fibre exits the tunnel crack, which is shortened because of the spalling, it bends around the intact matrix. This phenomenon is generally referred to as *snubbing effect*, and it is modelled through the frictional pulley idealisation [84], which complies with the fibre pull-out model adopted in the LDPM-F model [82]. In order to account for the snubbing effect, the fibre load is enlarged as follows:

$$P_f = P(v)\exp\left(k_{sn}\varphi_f'\right) \tag{28}$$

where k_{sn} is a dimensionless material parameter. The updated value of the fibre load must comply with the rupture strength of the fibre, then the following relationship must always hold:

$$\sigma_f = \frac{4P_f}{\pi d_f^2} \le \sigma_{u.f}\exp\left(-k_{rup}\varphi_f'\right) \tag{29}$$

in which k_{rup} is a material parameter, and $\sigma_{u.f}$ the ultimate tensile strength of the fibre. In case of fibre stress exceeding the corrected value of strength, P_f is set to zero. The exponential term in Eq. (29) reflects experimental evidence showing lower rupture loads in single fibre pull-out tests for increasing values of φ_f' [85].

Details about the model formulation can be found in Schauffert and Cusatis [60],Schauffert et al. [61].

Appendix C. Hygro-Thermo-Chemical model

Cement hydration degree. As demonstrated by several authors [86–88], the rate of the hydration degree, which describes the ratio between the amount of reacted cement and its total initial amount, can be expressed as

$$\dot{\alpha}_c = A_c(\alpha_c)\cdot\exp\left(-\frac{E_{a.c}}{RT}\right) \tag{30a}$$

$$A_c(\alpha_c) = A_{c.1}\left(A_{c.2} + \alpha_c\right)\left\langle\alpha_c^\infty - \alpha_c\right\rangle\cdot\exp\left(-\frac{\eta_c\alpha_c}{\alpha_c^\infty}\right) \tag{30b}$$

$$\alpha_c^\infty(h) = \tilde{\alpha}_c^\infty\exp\left[-\zeta_c\left(\frac{1}{h} - 1\right)\right] \tag{30c}$$

where $A_c(\alpha_c)$ is the normalised chemical affinity, $E_{a.c}$ is the hydration activation energy, R is the universal gas constant, and $A_{c.1}$, $A_{c.2}$, and η_c are material parameters. The hydration degree cannot decrease in time. For this reason, the Macaulay brackets $\langle x\rangle = \max(0, x)$ are used, in order to have $\dot{\alpha}_c \ge 0$ for $\forall t \ge 0$. The hydration rate slows down, or even stops, when relative humidity drops below a certain threshold [89], as described by Eq. (30)c.

Slag reaction degree. Similarly to the degree of cement hydration, being both diffusion-driven processes, the rate of the slag reaction degree is formulated by means of an Arrhenius-type law too.

$$\dot{\alpha}_{sl} = A_{sl}(\alpha_{sl}) \cdot \exp\left(-\frac{E_{a.sl}}{RT}\right) \tag{31a}$$

$$A_c(\alpha_{sl}) = A_{sl.1}\left(A_{sl.2} + \alpha_{sl}\right)\langle \alpha_{sl}^{\infty} - \alpha_{sl}\rangle \cdot \exp\left(-\frac{\eta_{sl}\alpha_{sl}}{\alpha_{sl}^{\infty}}\right) \tag{31b}$$

$$\alpha_{sl}^{\infty}(h) = \tilde{\alpha}_{sl}^{\infty} \exp\left[-\zeta_{sl}\left(\frac{1}{h} - 1\right)\right] \tag{31c}$$

$A_{sl}(\alpha_{sl})$ is the normalised chemical affinity, $E_{a.sl}$ the global reaction activation energy, α_{sl}^{∞} the asymptotic normalised reaction degree, and η_{sl}, $A_{sl.1}$, and $A_{sl.2}$ are material parameters to calibrate.

Evaporable water content. The evaporable water in the C-S-H gel, w_e^{gel}, and the capillary water, w_e^{cap}, formulations read

$$w_e^{gel} = g_2 \cdot \alpha\left(c \cdot \tilde{\alpha}_c^{\infty} + sl \cdot \tilde{\alpha}_{sl}^{\infty} \cdot \frac{\tilde{Q}_{sl}^{\infty}}{\tilde{Q}_c^{\infty}}\right) \cdot \left(1 - e^{-10\tilde{\alpha}_c^{\infty}(g_1 - \alpha)h}\right) \tag{32a}$$

$$w_e^{cap} = \frac{w_0 + \Delta w - w_n - w_e^{gel}\,(h = 1,00)}{e^{-10\tilde{\alpha}_c^{\infty}(g_1 - \alpha)} - 1} \tag{32b}$$

where Δw is made dependent on the ratio between the chemical shrinkage measured at full hydration for slag-based paste, $\Delta\tilde{w}_{sl}$, and Ordinary Portland Cement paste, $\Delta\tilde{w}_c$:

$$\Delta w = \kappa_{sh}\left(c \cdot \alpha_c + \frac{\Delta\tilde{w}_{sl}}{\Delta\tilde{w}_c} \cdot sl \cdot \alpha_{sl}\right) \tag{33}$$

Based on experimental data available in the literature, in this work, it is assumed $\Delta\tilde{w}_{sl} = 0.110$ mL/g_{slag} [90,91] and $\Delta\tilde{w}_c = 0.065$ mL/g_{cem} [40, 65]. If silica fume are added into the mixture, $\Delta\tilde{w}_s = 0.200$ mL/g_{SF} [40, 65].

Non-evaporable water content. It has been experimentally observed that both the hydration of Portland cement and the reaction of slag mineral admixtures contribute to chemically bound water w_n [92], for the computation of which an additive approach is followed:

$$\dot{w}_n = \kappa_c \cdot c \cdot \dot{\alpha}_c + \kappa_{sl} \cdot sl \cdot \dot{\alpha}_{sl} \tag{34}$$

where κ_c and κ_{sl} represent the mass ratios of non-evaporable water at full cement and slag hydration, respectively.

References

[1] B. Savija, Experimental and Numerical Investigation of Chloride Ingress in Cracked Concrete, Delft Univeristy of Technology, 2014.

[2] L. Shen, X. Yao, G. Di Luzio, M. Jiang, Y. Han, Mix optimization of hybrid steel and polypropylene fiber-reinforced concrete for anti-thermal spalling, J. Build. Eng. 63 (2023) 105409, http://dx.doi.org/10.1016/j.jobe.2022.105409, URL: https://www.sciencedirect.com/science/article/pii/S2352710222014152.

[3] A. Blagojević, the Influence of Cracks on the Durability and Service Life of Reinforced Concrete Structures in Relation to Chloride-Induced Corrosion: A Look from a Different Perspective, Delft Univeristy of Technology, 2016.

[4] S.C. Paul, G.P. van Zijl, B. Šavija, Effect of fibers on durability of concrete: A practical review, Materials 13 (20) (2020) http://dx.doi.org/10.3390/ma13204562.

[5] G. Di Luzio, L. Ferrara, V. Krelani, Numerical modeling of mechanical regain due to self-healing in cement based composites, Cem. Concr. Compos. 86 (2018) 190–205, http://dx.doi.org/10.1016/j.cemconcomp.2017.11.006.

[6] E. Cuenca, A. Mezzena, L. Ferrara, Synergy between crystalline admixtures and nano-constituents in enhancing autogenous healing capacity of cementitious composites under cracking and healing cycles in aggressive waters, Constr. Build. Mater. 266 (2021) 121447, http://dx.doi.org/10.1016/j.conbuildmat.2020.121447.

[7] A. de Souza Oliveira, O. da Fonseca Martins Gomes, L. Ferrara, E. de Moraes Rego Fairbairn, R. Toledo Filho, An overview of a twofold effect of crystalline admixtures in cement-based materials: from permeability-reducers to self-healing stimulators, J. Build. Eng. 41 (2021) 102400.

[8] N. De Belie, E. Gruyaert, A. Al-Tabbaa, P. Antonaci, C. Baera, D. Bajare, A. Darquennes, R. Davies, L. Ferrara, T. Jefferson, et al., A review of self-healing concrete for damage management of structures, Adv. Mater. Interfaces 5 (17) (2018) 1800074.

[9] M.M. Pelletier, Self-Healing Concrete (Ph.D. thesis), University of Rhode Island, 2010.

[10] V. Wiktor, H.M. Jonkers, Quantification of crack-healing in novel bacteria-based self-healing concrete, Cem. Concr. Compos. 33 (7) (2011) 763–770, http://dx.doi.org/10.1016/j.cemconcomp.2011.03.012.

[11] K. Van Tittelboom, N. De Belie, D. Van Loo, P. Jacobs, Self-healing efficiency of cementitious materials containing tubular capsules filled with healing agent, Cem. Concr. Compos. 33 (4) (2011) 497–505, http://dx.doi.org/10.1016/j.cemconcomp.2011.01.004.

[12] C. Dry, W. McMillan, Three-part methylmethacrylate adhesive system as an internal delivery system for smart responsive concrete, Smart Mater. Struct. 5 (3) (1996) 297–300, http://dx.doi.org/10.1088/0964-1726/5/3/007.

[13] C.M. Dry, Design of self-growing, self-sensing, and self-repairing materials for engineering applications, in: A.R. Wilson, H. Asanuma (Eds.), in: Smart Materials, 4234, International Society for Optics and Photonics, SPIE, 2001, pp. 23–29, http://dx.doi.org/10.1117/12.424430.

[14] C. Joseph, A.D. Jefferson, B. Isaacs, R. Lark, D. Gardner, Experimental investigation of adhesive-based self-healing of cementitious materials, Mag. Concr. Res. 62 (11) (2010) 831–843, http://dx.doi.org/10.1680/macr.2010.62.11.831.

[15] S. Sangadji, H. Schlangen, Porous network concrete: A new approach to make concrete structures self-healing using prefabricated porous layer, in: ICSHM 2011: Proceedings of the 3rd International Conference on Self-Healing Materials, Bath, UK, 27-29 June 2011, Citeseer, 2011.

[16] C.-M. Aldea, W.J. Song, J.S. Popovics, S.P. Shah, Extent of healing of cracked normal strength concrete, J. Mater. Civ. Eng. 12 (1) (2000) 92–96, http://dx.doi.org/10.1061/(ASCE)0899-1561(2000)12:1(92).

[17] L. Ferrara, V. Krelani, M. Carsana, A "fracture testing" based approach to assess crack healing of concrete with and without crystalline admixtures, Constr. Build. Mater. 68 (2014) 535–551, http://dx.doi.org/10.1016/j.conbuildmat.2014.07.008.

[18] C. Edvardsen, Water permeability and autogenous healing of cracks in concrete, ACI Mater. J. 96 (4) (1999) http://dx.doi.org/10.14359/645.

[19] H.-W. Reinhardt, M. Jooss, Permeability and self-healing of cracked concrete as a function of temperature and crack width, Cem. Concr. Res. 33 (7) (2003) 981–985, http://dx.doi.org/10.1016/S0008-8846(02)01099-2.

[20] F. Lo Monte, L. Ferrara, Self-healing characterization of UHPFRCC with crystalline admixture: Experimental assessment via multi-test/multi-parameter approach, Constr. Build. Mater. 283 (2021) 122579, http://dx.doi.org/10.1016/j.conbuildmat.2021.122579.

[21] E. Cuenca, L. D'Ambrosio, D. Lizunov, A. Tretjakov, O. Volobujeva, L. Ferrara, Mechanical properties and self-healing capacity of ultra high performance fibre reinforced concrete with alumina nano-fibres: Tailoring ultra high durability concrete for aggressive exposure scenarios, Cem. Concr. Compos. 118 (2021) 103956, http://dx.doi.org/10.1016/j.cemconcomp.2021.103956.

[22] E. Cuenca, V. Postolachi, L. Ferrara, Cellulose nanofibers to improve the mechanical and durability performance of self-healing ultra-high performance concretes exposed to aggressive waters, Constr. Build. Mater. 374 (2023) 130785, http://dx.doi.org/10.1016/j.conbuildmat.2023.130785.

[23] S. Fan, M. Li, X-ray computed microtomography of three-dimensional micro-cracks and self-healing in engineered cementitious composites, Smart Mater. Struct. 24 (1) (2014) 015021, http://dx.doi.org/10.1088/0964-1726/24/1/015021.

[24] L. Ferrara, P. Bamonte, C.S. Falcó, F. Animato, C. Pascale, A. Tretjakov, E.C. Torregrosa, P. Deegan, S. Sideri, E. Gastaldo-Brac, P. Serna, V. Mechtcherine, M. Alonso, A. Peled, R. Borg, An overview on H2020 project ReSHEALience, in: IABSE Symposium Towards a Resilient Built Environment - Risk and Asset Management, 27–29 March 2019 Guimaraes, Portugal, 2019, pp. 184–191.

[25] S. Al-Obaidi, P. Bamonte, M. Luchini, I. Mazzantini, L. Ferrara, Durability-based design of structures made with ultra-high-performance/ultra-high-durability concrete in extremely aggressive scenarios: Application to a geothermal water basin case study, Infrastructures 5 (11) (2020) 102.

[26] M.C. Caruso, C. Pascale, E. Camacho, L. Ferrara, Comparative environmental and social life cycle assessments of off-shore aquaculture rafts made in ultra-high performance concrete (UHPC), Int. J. Life Cycle Assess. 27 (2) (2022) 281–300, http://dx.doi.org/10.1007/s11367-021-02017-6.

[27] C. Schroefl, M. Reichardt, V. Mechtcherine, P. Deegan, Floating breakwater pontoon pilot cast with carbon textile reinforcement-based ultra high durability concrete: Materials development and testing, and implementation in the North Atlantic (Irelands west coast), MATEC Web Conf. 378 (2023) 08001, http://dx.doi.org/10.1051/matecconf/202337808001.

[28] A. Cibelli, L. Ferrara, G. Di Luzio, Mechanical aging of high slag content UHPC: experimental characterization and numerical modeling, Constr. Build. Mater. (2023) submitted for publication.

[29] T. Jefferson, E. Javierre, B. Freeman, A. Zaoui, E. Koenders, L. Ferrara, Research progress on numerical models for self-healing cementitious materials, Advanced Materials Interfaces 5 (17) (2018) 1701378, http://dx.doi.org/10.1002/admi.201701378.

[30] B. Hilloulin, F. Grondin, M. Matallah, A. Loukili, Modelling of autogenous healing in ultra high performance concrete, Cem. Concr. Res. 61 (2014) 64–70.

[31] B. Hilloulin, D. Hilloulin, F. Grondin, A. Loukili, N. De Belie, Mechanical regains due to self-healing in cementitious materials: Experimental measurements and micro-mechanical model, Cem. Concr. Res. 80 (2016) 21–32.

[32] A. Aliko-Benítez, M. Doblaré, J. Sanz-Herrera, Micromechanical modelling of self-healing cementitious materials, Int. J. Solids Struct. 69 (2015) 392–402.

[33] R. Davies, A. Jefferson, Chemical-diffusive modeling of the self-healing behavior in concrete, Int. J. Solids Struct. 113 (2017) 180–191.

[34] E. Barbero, F. Greco, P. Lonetti, Continuum damage-healing mechanics with application to self-healing composites, Int. J. Damage Mech. 14 (2005) 51–81.

[35] E. Schimmel, J. Remmers, Development of a constitutive model for self-healing materials, 2006, Report DACS-06-003, Delft Aerospace Computational Science.

[36] J. Mergheim, P. Steinmann, Phenomenological modelling of self-healing polymers based on integrated healing agents, Comput. Mech. 52 (3) (2013) 681–692.

[37] C. Oucif, G. Voyiadjis, T. Rabczuk, Modeling of damage-healing and nonlinear self-healing concrete behavior: Application to coupled and uncoupled self-healing mechanisms, Theor. Appl. Fract. Mech. 96 (2018) 216–230.

[38] Q. Chen, X. Liu, H. Zhu, J. Ju, X. Yongjian, Z. Jiang, Z. Yan, Continuum damage-healing framework for the hydration induced self-healing of the cementitious composite, Int. J. Damage Mech. 30 (5) (2021) 681–699.

[39] G. Di Luzio, G. Cusatis, Solidification–microprestress–microplane (SMM) theory for concrete at early age: Theory, validation and application, Int. J. Solids Struct. 50 (6) (2013) 957–975, http://dx.doi.org/10.1016/j.ijsolstr.2012.11.022.

[40] G. Di Luzio, G. Cusatis, Hygro-thermo-chemical modeling of high performance concrete. I: Theory, Cem. Concr. Compos. 31 (5) (2009) 301–308, http://dx.doi.org/10.1016/j.cemconcomp.2009.02.015.

[41] S. Yang, F. Aldakheel, A. Caggiano, P. Wriggers, E. Koenders, A review on cementitious self-healing and the potential of phase-field methods for modeling crack-closing and fracture recovery, MDPI Mater. 13 (22) (2020) 5265.

[42] A. Jefferson, B. Freeman, A crack-opening-dependent numerical model for self-healing cementitious materials, Int. J. Solids Struct. 244 (2022) 0020–7683.

[43] S.A. Ponnusami, J. Krishnasamy, S. Turteltaub, S. van der Zwaag, A cohesive-zone crack healing model for self-healing materials, Int. J. Solids Struct. 134 (2018) 249–263, http://dx.doi.org/10.1016/j.ijsolstr.2017.11.004, URL: https://www.sciencedirect.com/science/article/pii/S0020768317305024.

[44] B.L. Freeman, P. Bonilla-Villalba, I.C. Mihai, W.F. Alnaas, A.D. Jefferson, A specialised finite element for simulating self-healing quasi-brittle materials, Adv. Model. Simul. Eng. Sci. 7 (2020) http://dx.doi.org/10.1186/s40323-020-00171-4.

[45] A. Cibelli, M. Pathirage, G. Cusatis, L. Ferrara, G. Di Luzio, A discrete numerical model for the effects of crack healing on the behaviour of ordinary plain concrete: Implementation, calibration, and validation, Eng. Fract. Mech. 263 (2022) 108266, http://dx.doi.org/10.1016/j.engfracmech.2022.108266.

[46] L. Wan, R. Wendner, B. Liang, G. Cusatis, Analysis of the behavior of ultra high performance concrete at early age, Cem. Concr. Compos. 74 (2016) 120–135, http://dx.doi.org/10.1016/j.cemconcomp.2016.08.005.

[47] M. Alnaggar, G. Di Luzio, G. Cusatis, Modeling time-dependent behavior of concrete affected by alkali silica reaction in variable environmental conditions, Materials 10 (5) (2017) http://dx.doi.org/10.3390/ma10050471.

[48] W. Li, F. Bousikhane, J.W. Carey, G. Cusatis, Discrete modeling of the fracture-permeability behavior of shale, in: 51st US Rock Mechanics/Geomechanics Symposium, OnePetro, 2017.

[49] I. Boumakis, G. Di Luzio, M. Marcon, J. Vorel, R. Wan-Wendner, Discrete element framework for modeling tertiary creep of concrete in tension and compression, Eng. Fract. Mech. 200 (2018) 263–282, http://dx.doi.org/10.1016/j.engfracmech.2018.07.006.

[50] M. Pathirage, F. Bousikhane, M. D'Ambrosia, M. Alnaggar, G. Cusatis, Effect of alkali silica reaction on the mechanical properties of aging mortar bars: Experiments and numerical modeling, Int. J. Damage Mech. 28 (2) (2019) 291–322, http://dx.doi.org/10.1177/1056789517750213.

[51] H. Yin, A. Cibelli, S.-A. Brown, L. Yang, L. Shen, M. Alnaggar, G. Cusatis, G. Di Luzio, Flow lattice model for the simulation of chemistry dependent transport phenomena in cementitious materials, Eur. J. Environ. Civ. Eng. (2023) 1–25, http://dx.doi.org/10.1080/19648189.2023.2242456.

[52] J. Qiu, S. He, Q. Wang, H. Su, E. Yang, Autogenous healing of fiber/matrix interface and its enhancement, in: Proceedings of the 10St International Conference on Fracture Mechanics of Concrete and Concrete Structures, FraMCoS-X, 2019.

[53] A. Cibelli, G. Di Luzio, L. Ferrara, Numerical modelling via a coupled discrete approach of the autogenous healing for fibre-reinforced cementitious composites (FRCCs), in: Computational Modelling of Concrete and Concrete Structures EURO-C, Vienna, Austria, 2022, pp. 86–95.

[54] A. Cibelli, G. Di Luzio, L. Ferrara, Numerical modelling of the ageing of ultra high performance fibre reinforced cementitious composites, in: Proceedings of the 14th PhD Symposium in Civil Engineering, Rome, Italy, 2022, pp. 289–296.

[55] A. Cibelli, G. Di Luzio, L. Ferrara, Hygro-thermo-chemo-mechanical coupled discrete model for the self-healing in ultra high performance concrete, in: Life-Cycle of Structures and Infrastructure Systems IALCCE, Milan, Italy, 2023, pp. 1209–1216.

[56] G. Di Luzio, A. Cibelli, S. Al-Obaidi, S. Radwan, M. Davolio, L. Ferrara, R. Wan-Wendner, Y. Wang, Crack healing under sustained load in concrete: An experimental/numerical study, in: Life-Cycle of Structures and Infrastructure Systems IALCCE, Milan, Italy, 2023, pp. 1217–1224.

[57] G. Cusatis, D. Pelessone, A. Mencarelli, Lattice discrete particle model (LDPM) for failure behavior of concrete. I: Theory, Cem. Concr. Compos. 33 (9) (2011) 881–890, http://dx.doi.org/10.1016/j.cemconcomp.2011.02.011.

[58] G. Cusatis, A. Mencarelli, D. Pelessone, J. Baylot, Lattice discrete particle model (LDPM) for failure behavior of concrete. II: Calibration and validation, Cem. Concr. Compos. 33 (9) (2011) 891–905, http://dx.doi.org/10.1016/j.cemconcomp.2011.02.010.

[59] L. Han, M. Pathirage, A.T. Akono, G. Cusatis, Lattice discrete particle modeling of size effect in slab scratch tests, J. Appl. Mech. 88 (2) (2020) http://dx.doi.org/10.1115/1.4048989, 021009.

[60] E. Schauffert, G. Cusatis, Lattice discrete particle model for fiber-reinforced concrete. I: Theory, J. Eng. Mech. 138 (7) (2012) 826–833.

[61] E. Schauffert, G. Cusatis, D. Pelessone, J. O'Daniel, J. Baylot, Lattice discrete particle model for fiber-reinforced concrete. II: Tensile fracture and multiaxial loading behavior, J. Eng. Mech. 138 (7) (2012) 834–841.

[62] R. Rezakhani, D.A. Scott, F. Bousikhane, M. Pathirage, R.D. Moser, B.H. Green, G. Cusatis, Influence of steel fiber size, shape, and strength on the quasi-static properties of ultra-high performance concrete: Experimental investigation and numerical modeling, Constr. Build. Mater. 296 (2021) 123532, http://dx.doi.org/10.1016/j.conbuildmat.2021.123532.

[63] M. Abdellatef, M. Alnaggar, G. Boumakis, G. Cusatis, G. Di Luzio, R. Wendner, Lattice discrete particle modeling for coupled concrete creep and shrinkage using the solidification microprestress theory, in: 10th Conference on Mechanics and Physics of Creep, Shrinkage and Durability of Concrete and Concrete Structures, CONCREEP 10, 21–23 September 2015 Vienna, Austria, 2015, pp. 184–193.

[64] D.P. Bentz, CEMHYD3D: A three-dimensional cement hydration and microstructure development modeling package. Version 3.0., 2005, http://dx.doi.org/10.6028/NIST.IR.7232.

[65] G. Di Luzio, G. Cusatis, Hygro-thermo-chemical modeling of high-performance concrete. II: Numerical implementation, calibration, and validation, Cem. Concr. Compos. 31 (5) (2009) 309–324, http://dx.doi.org/10.1016/j.cemconcomp.2009.02.016.

[66] M. Pathirage, D. Bentz, G. Di Luzio, E. Masoero, G. Cusatis, The ONIX model: a parameter-free multiscale framework for the prediction of self-desiccation in concrete, Cem. Concr. Compos. 103 (2019) 36–48, http://dx.doi.org/10.1016/j.cemconcomp.2019.04.011.

[67] Z. Bažant, L. Najjar, Nonlinear water diffusion in nonsaturated concrete, Matér. Constr. 5 (1) (1972) 3–20, http://dx.doi.org/10.1007/BF02479073.

[68] S. Al-Obaidi, S. He, E. Schlangen, L. Ferrara, Effect of matrix self-healing on the bond-slip behavior of micro steel fibers in ultra-high-performance concrete, Mater. Struct. 56 (9) (2023) 161, http://dx.doi.org/10.1617/s11527-023-02250-5.

[69] J. Han, M. Zhao, J. Chen, X. Lan, Effects of steel fiber length and coarse aggregate maximum size on mechanical properties of steel fiber reinforced concrete, Constr. Build. Mater. 209 (2019) 577–591, http://dx.doi.org/10.1016/j.conbuildmat.2019.03.086.

[70] F. Lo Monte, L. Ferrara, Tensile behaviour identification in ultra-high performance fibre reinforced cementitious composites: indirect tension tests and back analysis of flexural test results, Mater. Struct. 53 (6) (2020) 145, http://dx.doi.org/10.1617/s11527-020-01576-8.

[71] S. Al-Obaidi, M. Davolio, G. Recchia, F. Lo Monte, L. Ferrara, How does self-healing under sustained loadings in aggressive water affect the constitutive response of a UHPFRC? in: 5th International Workshop on Strain Hardening Cementitious Composites, SHCC5, RILEM, 2022, pp. 239–248.

[72] A. Cibelli, Computational Modelling of Ageing, Healing and Degradation of Ordinary and Ultra High Performance Concrete (Ph.D. thesis), Politecnico di Milano, Milan, Italy, 2022.

[73] J. Smith, G. Cusatis, D. Pelessone, E. Landis, J. O'Daniel, J. Baylot, Discrete modeling of ultra-high-performance concrete with application to projectile penetration, Int. J. Impact Eng. 65 (2014) 13–32, http://dx.doi.org/10.1016/j.ijimpeng.2013.10.008.

[74] M. Alnaggar, G. Cusatis, Automatic parameter identification of discrete mesoscale models with application to the coarse-grained simulation of reinforced concrete structures, in: 20th Analysis and Computation Specialty Conference, 2012, pp. 406–417, http://dx.doi.org/10.1061/9780784412374.036.

[75] L. Ferrara, N. Ozyurt, M. di Prisco, High mechanical performance of fibre reinforced cementitious composites: the role of "casting-flow induced"fibre orientation, Mater. Struct. 44 (1) (2011) 109–128, http://dx.doi.org/10.1617/s11527-010-9613-9.

[76] B. Hughes, N. Fattuhi, Stress-strain curves for fibre reinforced concrete in compression, Cem. Concr. Res. 7 (2) (1977) 173–183, http://dx.doi.org/10.1016/0008-8846(77)90028-X.

[77] A. Hassan, S. Jones, G. Mahmud, Experimental test methods to determine the uniaxial tensile and compressive behaviour of ultra high performance fibre reinforced concrete (UHPFRC), Constr. Build. Mater. 37 (2012) 874–882, http://dx.doi.org/10.1016/j.conbuildmat.2012.04.030, Non Destructive Techniques for Assessment of Concrete.

[78] S.C. Lee, J.H. Oh, J.Y. Cho, Compressive behavior of fiber-reinforced concrete with end-hooked steel fibers, Materials 8 (4) (2015) 1442–1458, http://dx.doi.org/10.3390/ma8041442.

[79] A. Cibelli, G. Di Luzio, L. Ferrara, Numerical simulation of the chloride penetration in cracked and healed UHPC via a discrete multiphysics model, J. Eng. Mech. (2023) http://dx.doi.org/10.1061/JENMDT/EMENG-7188.

[80] S. Al-Obaidi, P. Bamonte, F. Animato, F. Lo Monte, I. Mazzantini, M. Luchini, S. Scalari, L. Ferrara, Innovative design concept of cooling water tanks/basins in geothermal power plants using ultra-high-performance fiber-reinforced concrete with enhanced durability, Sustainability 13 (17) (2021) http://dx.doi.org/10.3390/su13179826.

[81] Z. Lin, T. Kanda, V.C. Li, On interface property characterization and performance of fiber reinforced cementitious composites, J. Concrete Science and Engineering, RILEM 1 (1999) 173–184.

[82] E.H. Yang, S. Wang, Y. Yang, V.C. Li, Fiber-bridging constitutive law of engineered cementitious composites, J. Adv. Concr. Technol. 6 (1) (2008) 181–193, http://dx.doi.org/10.3151/jact.6.181.

[83] Z. Lin, V.C. Li, Crack bridging in fiber reinforced cementitious composites with slip-hardening interfaces, J. Mech. Phys. Solids 45 (5) (1997) 763–787, http://dx.doi.org/10.1016/S0022-5096(96)00095-6.

[84] V. Li, Y. Wang, S. Backer, Effect of inclining angle, bundling and surface treatment on synthetic fibre pull-out from a cement matrix, Composites 21 (2) (1990) 132–140, http://dx.doi.org/10.1016/0010-4361(90)90005-H.

[85] T. Kanda, V.C. Li, Interface property and apparent strength of high-strength hydrophilic fiber in cement matrix, J. Mater. Civ. Eng. 10 (1) (1998) 5–13, http://dx.doi.org/10.1061/(ASCE)0899-1561(1998)10:1(5).

[86] F.J. Ulm, O. Coussy, Modeling of thermochemomechanical couplings of concrete at early ages, J. Eng. Mech. 121 (7) (1995) 785–794, http://dx.doi.org/10.1061/(ASCE)0733-9399(1995)121:7(785).

[87] M. Cervera, J. Oliver, T. Prato, Thermo-chemo-mechanical model for concrete. I: Hydration and aging, J. Eng. Mech. 125 (9) (1999) 1018–1027, http://dx.doi.org/10.1061/(ASCE)0733-9399(1999)125:9(1018).

[88] E. Masoero, G. Cusatis, G. Di Luzio, C–S–H gel densification: The impact of the nanoscale on self-desiccation and sorption isotherms, Cem. Concr. Res. 109 (2018) 103–119, http://dx.doi.org/10.1016/j.cemconres.2018.04.014.

[89] Z.P. Bažant, S. Prasannan, Solidification theory for concrete creep. I: Formulation, J. Eng. Mech. 115 (8) (1989) 1691–1703, http://dx.doi.org/10.1061/(ASCE)0733-9399(1989)115:8(1691).

[90] J.J. Thomas, A.J. Allen, H.M. Jennings, Density and water content of nanoscale solid C–S–H formed in alkali-activated slag (AAS) paste and implications for chemical shrinkage, Cem. Concr. Res. 42 (2) (2012) 377–383, http://dx.doi.org/10.1016/j.cemconres.2011.11.003.

[91] C. Cartwright, F. Rajabipour, A. Radlińska, Shrinkage characteristics of alkali-activated slag cements, J. Mater. Civ. Eng. 27 (7) (2015) B4014007, http://dx.doi.org/10.1061/(ASCE)MT.1943-5533.0001058.

[92] X.Y. Wang, H.S. Lee, Modeling the hydration of concrete incorporating fly ash or slag, Cem. Concr. Res. 40 (7) (2010) 984–996, http://dx.doi.org/10.1016/j.cemconres.2010.03.001.